https://doi.org/10.1016/j.camwa.2018.04.020 This is the Pre-Published Version.

An improved k-ω-φ-α turbulence model applied to near-wall, separated and impinging jet flows and heat transfer

X.L. Yang

College of Civil Engineering, Shenzhen University, Shenzhen 518060, P.R. China.

Corresponding author

Y. Liu

Department of Mechanical Engineering, The Hong Kong Polytechnic University, Hung Hom, Kowloon, Hong Kong.

e-mail: yang.liu@polyu.edu.hk

An improved *k-ω-φ-α* turbulence model applied to near-wall, separated and impinging jet flows and heat transfer

Abstract: A turbulence model based on elliptic blending concept, referred to as improved $k-\omega-\varphi-\alpha$ model compared against the original $k-\omega-\varphi-\alpha$ model developed previously, is developed and verified. This model consists of four governing equations. Among them the k and ω equations are based on the Wilcox's $k-\omega$ model with some modifications and improvements according to the original $k-\omega-\varphi-\alpha$ model, and the φ and α equations are extracted from the original $k-\omega-\varphi-\alpha$ model directly without any change. The improved $k-\omega-\varphi-\alpha$ model is applied to near-wall, separated and impinging jet flows and convective heat transfer, i.e. the 2D fully developed channel flow, the 2D backward-facing step flow, the 2D impinging jet flow, and the convective heat transfer in the 2D fully developed channel flow and the 2D impinging jet flow. The computational results are compared with available DNS and experimental data and also to those computed using the original $k-\omega-\varphi-\alpha$ model and the popular Menter's SST $k-\omega$ model. It is shown that the improved $k-\omega-\varphi-\alpha$ model has better numerical stability, higher computational efficiency and more concise form than the original $k-\omega-\varphi-\alpha$ model. In addition, compared with the original $k-\omega-\varphi-\alpha$ model, the improved $k-\omega-\varphi-\alpha$ model can yield similar velocity profiles in the fully developed channel flow and step flow and friction and pressure coefficients in the step flow and very close temperature profiles in the fully developed channel flow. Moreover, it shows significant improvements on the predictions for the fluid flow and heat transfer in the impinging jet flow. As a whole, the improved $k-\omega-\varphi-\alpha$ model predicts better results than both of the original $k-\omega-\varphi-\alpha$ model and the SST $k-\omega$ model.

Keywords: turbulence model; elliptic blending; near-wall flow; separated flow; impinging jet flow; convective heat transfer.

Nomenclature

Greek letters

α Elliptic variable

$\beta, \gamma, \beta^*, \beta_0$ Turbulence model coefficients

δ Half width of the channel

$\varepsilon, \varepsilon_h$ Dissipation rate and homogeneous dissipation rate

ω, ω_h Specific dissipation rate and homogeneous specific dissipation rate

κ Von Karman constant

μ, ν Molecular dynamic and kinematic viscosity

μ_t, ν_t Turbulent dynamic and kinematic viscosity

Ω_{ij} Vorticity rate tensor

φ Wall-normal turbulent anisotropy, $\varphi = \overline{v^2}/k$

ρ Density of fluid

$\sigma_d, \sigma_{d0}, \sigma_{d1}$ Turbulence model constants

$\sigma_k, \sigma_\omega, \sigma_\varepsilon, \sigma_\varphi$ Turbulent Prandtl numbers

τ, τ_w Shear stress and wall shear stress

θ Mean temperature of the fluid

θ_w Wall temperature

θ_{in} Fluid temperature at inlet

θ^+ The normalized temperature

ζ Turbulence model constant

Latin letters

B Width of the inlet of the jet

C_f Skin-friction coefficient

C_p Pressure coefficient

c_p Specific heat of the fluid

$C_{\varepsilon 1}, C^*_{\varepsilon 1}, C_{\varepsilon 2}, C^*_{\varepsilon 2}\ C_{\varepsilon 3}, C_{\varepsilon 4}, C_{\varepsilon 5}\ C_\mu, C_T, C_\eta, C_1, C_2$ Turbulence model parameters

C_D Cross-diffusion term

D_k, D^t_k Turbulent diffusion of k

E The 'E' term

f Elliptic relaxation function

f_k, f_ω Damping functions

f_β Additional function

F_b Blending function

G_k Production of turbulent kinetic energy

H Step height

I Turbulent intensity

k Turbulent kinetic energy or thermal conductivity of the fluid

L Turbulence length scale

n Turbulence model constant

Nu Nusselt number

p Pressure or turbulence model constant

Pr Molecular Prandtl number

Pr_t turbulent Prandtl number

q Heat flux

Re_H Reynolds number based on H

Re_t Turbulent Reynolds number

Re_τ Friction velocity based Reynolds number

S Magnitude of strain rate

S_{ij} Strain rate tensor

t Physical time

T Turbulence time scale

$T_{\lim}$ Upper bound of the turbulence time scale

u_i Instantaneous velocity vector

u, v, w Velocities along x, y and z directions

U_b Mean velocity of the bulk flow

u^+ Normalized velocity by friction velocity

u_τ Friction velocity, $u_\tau = \sqrt{\tau_w / \rho}$

V_0 Mean velocity on the inlet of the jet

$\overline{v^2}$ Velocity variance scale

x Coordinate in the stream-wise direction

y Wall distance or coordinate in the wall-normal direction

y^+ Non-dimensional wall distance

1. Introduction

Accurately predicting turbulent information is of importance from practical and theoretical points of view because turbulent flows are commonly encountered in engineering applications. It is well known that the Direct Numerical Simulation (DNS) can solve directly the Navier-Stokes (N-S) equations, which are able to describe the details of turbulent motions, without any simplification. However, its huge computing capacity prevents it from being applied in real engineering problems. Alternatively, the Reynolds-Averaged N-S equations (corresponding to RANS methods) and the filtered

N-S equations (corresponding to Large Eddy Simulation method, LES) are primarily utilized in practices. Although LES shows more powerful ability than RANS for turbulence simulation, especially for unsteady turbulent flows, its application range is limited just for problems without wall effects or wall bounded flow with low Reynolds number and limited domain because of the shortcoming of LES laying in the high resolution requirements in wall boundary layers. In recent years, the hybrid RANS-LES approaches become increasingly popular: to name but a few, the Detached Eddy Simulation (DES) method was developed and improved by Spalart et al. [2], the Zonal Large Eddy Simulation (ZLES) method was developed by Quemere et al. [3], and the Scale-Adaptive Simulation (SAS) method was firstly developed by Menter and Egorov [4]. The hybrid RANS-LES approaches utilise the RANS method to model the turbulence near the wall, and restore to the LES ability in the regions far away from the wall or in the regions with massive separations. The major benefit of the hybrid RANS-LES methods is that they offer a nice compromise between the computational costs and the accuracy of the calculated results. Not only for the purpose of using the RANS methods to simulate the complex turbulent flows, but also for the development of the hybrid RANS-LES method, the refined modelling of wall effects in the framework of RANS is continually significant.

The interest in the $\overline{v^2} - f$ model, which belongs to one of the RANS framework turbulence models, has increased since the $\overline{v^2} - f$ model was firstly introduced in 1991 by Durbin [5]. The $\overline{v^2} - f$ model chooses a proper velocity scale, $\sqrt{\overline{v^2}}$, instead of $\sqrt{k}$, thus being able to predict the eddy viscosity in the near wall region more correctly without any damping function.

A notable number of researches have been carried out to improve the accuracy and robustness of the $\overline{v^2}-f$ model over the past 25 years, leading to several versions of $\overline{v^2}-f$ model. On the whole, the developments of the $\overline{v^2}-f$ model can be divided into two categories: one stems from the $k-\varepsilon$ system, another stems from the $k-\omega$ system. The evolution of the $\overline{v^2}-f$ model based on the $k-\varepsilon$ system had been reviewed by Billard and Laurence [6] in detail. They drew a conclusion that it is difficult to give considerations to both stability and accuracy. Then, they developed a new model (denoted as BL$-\overline{v^2}/k$ model) which not only keeps the robustness of some $\overline{v^2}-f$ models, but also improves the model predictions for some particular turbulent behaviour. This model uses the wall-normal anisotropy, $\varphi=\overline{v^2}/k$, and another parameter resulting from an elliptic equation, α, to blend the homogeneous and near-wall limiting expressions of f. The advantage is that the stiffness coming from the boundary condition of f, encountered in several versions of the $\overline{v^2}-f$ model, can be effectively eliminated. Moreover, a functional coefficient $C_{\varepsilon 2}^{*}$ was constructed to increase the turbulent dissipation in the defect layer, thus tackling the problem of over-estimation of the turbulent viscosity occurring in most of the $k-\varepsilon$ models with constant value of $C_{\varepsilon 2}$. Additionally, the 'E' term, which was originally proposed in the ε equation to account for the viscous wall effects by Jones and Launder [7] but was abandoned later by Thielen et al. [8] because of the numerical difficulties, was reintroduced to retard turbulence growth in the buffer layer. This term was ingeniously moved to the k equation so that it can be solved implicitly, thus no numerical difficulty still exists. The BL$-\overline{v^2}/k$ model has been utilized successfully in a few of 2D and 3D flows and has been proved to strike good balance between stability and accuracy [6, 9].

The $\overline{v^2}-f$ models stemming from the $k-\varepsilon$ system have a major drawback associated with the wall boundary condition of ε, especially the unreasonable initial value of ε [1]. From a practical point of view, it was generally suggested to begin the calculation using one of the $k-\varepsilon$ models until a convergent solution is achieved, then switch to the $\overline{v^2}-f$ model [10]. This means the problem may be solved twice in order to obtain a converged $\overline{v^2}-f$ solution and excessively computational capacity may be required. Another category of the $\overline{v^2}-f$ model, which is based on the $k-\omega$ system, can tackle this problem to some degree. The first $k-\omega$ based $\overline{v^2}-f$ model we found in literatures was developed by Jones in 2003 [11]. This model stems from a $\overline{v^2}-f$ model based on the $k-\varepsilon$ system by using the transformation of $\varepsilon=\beta^*\omega k^n\left(\overline{v^2}\right)^{1-n}$. Taha [12] developed a $k-\omega-\overline{v^2}-f$ model based on the Wilcox's standard $k-\omega$ model [13] and the $\overline{v^2}-f$ model of Lien and Kalitzin [14] and validated it through applying to the fully developed channel flow and the asymmetric plane diffuser flow. Later, this model was successfully used to simulate the unsteady flows around bluff bodies by Nazari et al. [15] and to evaluate the convective heat transfer around two side by side square cylinders by Mirzaei and Sohankar [16]. Khalaji et al. [17] developed a new $k-\omega-\overline{v^2}-f$ model based on the latest version of Wilcox's $k-\omega$ model [18] (denoted as Wilcox's $k-\omega$ model hereafter) and the $\overline{v^2}-f$ model of Lien and Kalitzin [14]. This model was used for simulations of the 2D impinging jet flow on flat surface [17] and concave surface [19], and acceptable results were obtained. Recently, the authors developed a $k-\omega-\varphi-\alpha$ model (referred to as the original $k-\omega-\varphi-\alpha$ model later) based on the Wilcox's $k-\omega$ model and the BL$-\overline{v^2}/k$ model. In this model, the k and ω equations

retain the formulations of the Wilcox's $k-\omega$ model in the near wall region and take the formulations transformed from the $\mathrm{BL}-\overline{v^2}/k$ model elsewhere. The φ and α equations are extracted from the $\mathrm{BL}-\overline{v^2}/k$ model directly. This model was applied to the 2D fully developed channel flow and 2D separation flows. The results showed that this model can yield flow predictions as accurate as the $\mathrm{BL}-\overline{v^2}/k$ model, and better numerical stability as well [1].

Up to now, comparing to the $\overline{v^2}-f$ models based on the $k-\varepsilon$ system, the $k-\omega$ system based $\overline{v^2}-f$ models are really underdeveloped and their applications are not popular. More importantly, we find that our original $k-\omega-\varphi-\alpha$ model has a drawback that it is difficult to achieve convergent solution in the case with very low turbulent intensity. Additionally, it can not predict fluid flow and heat transfer in the impinging jet well. Moreover, some terms in the original $k-\omega-\varphi-\alpha$ model are not so important and they can be dropped out to improve computational efficiency of the model. Therefore, in present paper, an improved $k-\omega-\varphi-\alpha$ turbulence model is developed. Then this model is validated using the near-wall, separated and impinging jet flows and convective heat transfer, and the numerical stability and the computational efficiency are also investigated.

The present paper is organised as follows. The development of the model is described in Section 2 in detail. The numerical procedure is introduced in Section 3. In Section 4, the performance of the model in the 2D fully developed channel flow, the 2D backward-facing step flow, the 2D impinging jet flow, and the convective heat transfer is investigated. The numerical stability and the computational efficiency of the model are also studied. Some conclusions are drawn in Section 5.

2. Development of the model

The improved $k-\omega-\varphi-\alpha$ turbulence model can be considered as an improved version of the original $k-\omega-\varphi-\alpha$ model. For the sake of convenient reference, the original $k-\omega-\varphi-\alpha$ model is listed briefly in following.

$$\frac{\partial \rho k}{\partial t}+\frac{\partial}{\partial x_i}\left(\rho u_i k\right)=G_k-\rho\beta^{*}{}'k\omega-E+\frac{\partial}{\partial x_j}\left[\left(\frac{\mu}{2}+\sigma_k\mu_t\right)\frac{\partial k}{\partial x_j}\right], \tag{1}$$

$$\frac{\partial \rho \omega}{\partial t}+\frac{\partial}{\partial x_i}\left(\rho u_i \omega\right)=\gamma\frac{\omega}{k}G_k-\rho\beta\omega^2+C_D-F_bD_k+\frac{\partial}{\partial x_j}\left[\left(\frac{\mu}{2}+\sigma_\omega\mu_t\right)\frac{\partial \omega}{\partial x_j}\right], \tag{2}$$

$$\frac{\partial \rho \varphi}{\partial t}+\frac{\partial}{\partial x_i}\left(\rho u_i \varphi\right)=\left(1-\alpha^p\right)\rho f_{wall}+\alpha^p\rho f_{\hom}-\frac{\varphi}{k}G_k+\frac{2}{k}\mu_t\sigma_k\frac{\partial \varphi}{\partial x_j}\frac{\partial k}{\partial x_j}+\frac{\partial}{\partial x_j}\left[\left(\frac{\mu}{2}+\sigma_\varphi\mu_t\right)\frac{\partial \varphi}{\partial x_j}\right], \tag{3}$$

$$0=\frac{1-\alpha}{L^2}+\frac{\partial}{\partial x_j}\left(\frac{\partial \alpha}{\partial x_j}\right), \tag{4}$$

where the 'E' term reads

$$E=2C_{\varepsilon 3}\left(1-\alpha\right)^p\frac{1}{\beta^{*}\omega}\frac{\mu\mu_t}{\rho}\left(\frac{\partial^2 u_i}{\partial x_j\partial x_k}\right)^2, \tag{5}$$

the cross-diffusion term reads

$$C_D=\left[F_b\frac{2}{k}\left(\frac{\mu}{2}+\mu_t\sigma_{\omega 1}\right)\frac{\partial k}{\partial x_j}\frac{\partial \omega}{\partial x_j}+\left(1-F_b\right)\sigma_d\frac{\rho}{\omega}\max\left(\frac{\partial k}{\partial x_j}\frac{\partial \omega}{\partial x_j},0.0\right)\right], \tag{6}$$

and another diffusion term in the ω equation is

$$D_k=\left(\sigma_{k1}-\sigma_{\omega 1}\right)\frac{\omega}{k}\frac{\partial}{\partial x_j}\left(\mu_t\frac{\partial k}{\partial x_j}\right). \tag{7}$$

For the sake of brevity, the definitions of other terms are not listed here and they can be found in [1].

2.1 Simplification of the k and ω equations

In the *k* equation of the original $k-\omega-\varphi-\alpha$ model (Equation (1)), there is an 'E' term, which was originally used by Jones and Launder [7] to model the $P_{\varepsilon 3}$ term appearing in the exact ε transport equation. This term plays an role in the buffer layer of the attached boundary layer. However, this term is known to be numerically stiff due to the second order derivatives. Manceau and Hanjalic [20] replaced this term using a variable $C_{\varepsilon 1}$ coefficient. However, there are no clear physical justifications even though it is easier to be computed. Billard and Laurence [6, 21] reintroduced the 'E' term into the $\mathrm{BL}-\overline{v^2}/k$ model, but they moved this term from the ε equation to the k equation. The major benefit is that this term having the form '$-k\times\cdots$' in the k equation allows implicit discretization, thus improving numerical stability. However, as demonstrated by Yang et al. [1], when the turbulent equations are transformed to the $k-\omega$ system, this benefit has been lost because this term will be handled explicitly in the k equation again. Though this term does not induce any problem in the original $k-\omega-\varphi-\alpha$ model for simple 2D flows, it is hard to say this term will not none the less induce numerical difficulty for complex 3D flows. What's more, as shown in Section 4.4, the '*E*' term has significantly undesirable influence on the impinging jet flow and delays the secondary maxima of the wall friction force and the Nusselt number too much. Consequently, in the improved $k-\omega-\varphi-\alpha$ model, the 'E' term is removed. Fortunately, we find that, with remedy by re-adjusting other terms in the $k-\omega$ system, the re-movement of this term does not reduce the accuracy of the improved $k-\omega-\varphi-\alpha$ model in the buffer layer of the channel flow (see Section 4.1).

In the ω equation of the original $k-\omega-\varphi-\alpha$ model, there is a 'D_k' term (Equation (7)), which comes from the procedure of transforming the $k-\varepsilon$ system to the $k-\omega$ system. The major reason of keeping this term in the original $k-\omega-\varphi-\alpha$ model is to avoid adjusting too many parameters. Though this term does not increase any

complexity of the model, it increases the computational consume definitely. Actually, this term is very small comparing to other terms in the ω equation. This feature can be illustrated in Fig. 1, in which the non-dimensional 'D_k' term is compared with the cross-diffusion term 'C_D' for channel flow at $\mathrm{Re}_\tau = 1000$ (both terms are computed using the original $k-\omega-\varphi-\alpha$ model and normalized by $\rho k_0 / h^2$, where k_0 is the mean turbulent kinetic energy at inlet section and h is the half width of the channel). It can be seen that the ratio of the maximum absolute values of the 'D_k' term to the 'C_D' term is only about 1%. Consequently, in present model, this term is reasonably neglected under the remedy of re-adjusting some parameters, just as the baseline and SST $k-\omega$ model of Menter [22].

In the k and ω equations (Equation (1) and (2)) of the original $k-\omega-\varphi-\alpha$ model , some of the model parameters are computed using a blending function F_b as

$$\phi = F_b \phi_1 + (1 - F_b)\phi_2 , \tag{8}$$

where ϕ represents the five new model parameters (β^{*}', σ_k, γ, β and σ_ω), ϕ_1 and ϕ_2 represent corresponding parameters in the transformed $k-\omega$ model (used in the region far away from the wall) and the Wilcox's $k-\omega$ model (used in the near wall region), respectively. Actually, this treatment is not essential for advanced turbulence models. For example, the Wilcox's $k-\omega$ model uses unified model parameters in all flow regions and achieves great success yet. In the improved $k-\omega-\varphi-\alpha$ model, the thinking of 'blending function' is not used in the k and ω equations and unified model parameters are adopted.

After dropping out the 'E' term in the k equation (Equation (1)) and the 'D_k' term in the ω equation (Equation(2)), and adopting unified model parameters in all flow regions, the k and ω equations become to have more concise form and they are similar to those in the Wilcox's $k-\omega$ model. Considering the model parameters in the

Wilcox's $k-\omega$ model has been optimized, most of them are adopted in the improved $k-\omega-\varphi-\alpha$ model. From this point of view, also for the sake of convenient description, the k and ω equations in the improved $k-\omega-\varphi-\alpha$ model can be considered as improved analogues deriving from the Wilcox's $k-\omega$ model with some modifications and improvements according to the original $k-\omega-\varphi-\alpha$ model. The modifications and improvements will be described below in detail. For reference, the k and ω equations of the Wilcox's $k-\omega$ model are given as

$$\frac{\partial \rho k}{\partial t}+\frac{\partial}{\partial x_i}\left(\rho u_i k\right)=G_k-\rho\beta^* k\omega+\frac{\partial}{\partial x_j}\left[\left(\mu+\sigma_k\mu_t\right)\frac{\partial k}{\partial x_j}\right], \tag{9}$$

$$\frac{\partial \rho \omega}{\partial t}+\frac{\partial}{\partial x_i}\left(\rho u_i \omega\right)=\gamma\frac{\omega}{k}G_k-\rho\beta\omega^2+\max\left(\sigma_d\frac{\rho}{\omega}\frac{\partial k}{\partial x_j}\frac{\partial \omega}{\partial x_j},0.0\right)+\frac{\partial}{\partial x_j}\left[\left(\mu+\sigma_\omega\mu_t\right)\frac{\partial \omega}{\partial x_j}\right], \tag{10}$$

where $\beta=\beta_0 f_\beta$. The function f_β is used to resolve the plane-jet/round-jet anomaly occurring in the Wilcox's $k-\omega$ model. It should be noted that, in the improved $k-\omega-\varphi-\alpha$ model, it is found that the plane-jet/round-jet anomaly does not remain (for the sake of brevity, the detailed results are not shown in present paper), so that the f_β function is not needed and $f_\beta=1$ is adopted for all problems.

2.2 Modification of the molecular diffusion

It can be seen that in the diffusion term of the original $k-\omega-\varphi-\alpha$ model (the last terms on the right hand side of Equations (1-3)), the molecular diffusion coefficient is $\mu/2$. This expression is derived from the BL-$\overline{v^2}/k$ model [21], in which the homogenous dissipation rate (defined as $\varepsilon_h=\varepsilon-0.5\nu\Delta k$) is solved instead of ε. For consistency, the dissipation rate in all equations (k, ε and φ equations) is replaced by the homogenous

dissipation rate. Jakirlic and Hanjalic [23] predicted that the unique modification is that the molecular diffusion effect in all corresponding terms should be halved after neglecting higher order terms, namely, the molecular diffusion coefficient in all equations should be divided by two.

Jakirlic and Hanjalic [23] also showed that a consistent use of ε_h and the components of the stress dissipation rate tensor can provide several benefits, such as satisfaction of wall limits without any wall topography parameter, reducing the necessity for empirical inputs and enabling better term by term reproduction of DNS data. The same advantages can be taken in the $k-\omega$ model by solving $\omega_h = \varepsilon_h/(\beta^* k)$ instead of ω [24]. After transforming ε_h equation to the ω_h equation by using $\omega_h = \varepsilon_h/(\beta^* k)$, it is easy to show that, after neglecting some unimportant higher order terms, the resulting ω_h equation has the same form as Equation (9) with unique variation of the molecular diffusion to be $\mu/2$. Therefore, in present model, the molecular diffusion coefficient in the k and ω equations (Equations (9) and (10)) becomes as $\mu/2$.

For simplicity, we use notations 'ε' and 'ω' to represent ε_h and ω_h respectively in the following, unless special declaration is provided.

2.3 Modification of the coefficient β_0

The same modification of the coefficient β_0 as in the original $k-\omega-\varphi-\alpha$ model is taken. It reads

$$\beta_0 = (C_{\varepsilon 2}^* - 1)\beta^*, \tag{11}$$

where

$$C_{\varepsilon 2}^* = C_{\varepsilon 2} + \alpha^p \left(C_{\varepsilon 4} - C_{\varepsilon 2}\right) \tanh\left[\max\left(\frac{D_k^t}{\beta^* k\omega}, 0\right)\right]. \tag{12}$$

and $D_k^t = \partial\left(\sigma_k \nu_t \partial k/\partial x_j\right)/\partial x_j$.

This modification is important because it enables β_0 to take a smaller value where the ratio $D_k^t/\left(\beta^* k\omega\right)$ is significant (for example, in the defect layer of the channel flow), further resulting in increase of ω, thus decreasing the k and μ_t ($\mu_t \propto k/\omega$) and improving the velocity predictions.

2.4 Modification of the coefficient γ

Another modification is made on the coefficient γ, which affects the shear layer spreading rate significantly. From the procedure of transforming the ε equation to the ω equation, it is easy to find that $\gamma = C_{\varepsilon 1} - 1$. On the other hand, Wilcox showed that in log-layer the relation of $\gamma = \beta_0/\beta^* - \kappa^2\sigma_\omega/\sqrt{\beta^*}$ should be held in the $k-\omega$ model [13]. In the log-layer, $C_{\varepsilon 2}^* = C_{\varepsilon 2}$, so that Equation (11) becomes $\beta_0/\beta^* = C_{\varepsilon 2} - 1$. Consequently, the following relation can be derived

$$C_{\varepsilon 1} = C_{\varepsilon 2} - \kappa^2\sigma_\omega/\sqrt{\beta^*}\,. \tag{13}$$

If Equation (13) (i.e. a constant value of $C_{\varepsilon 1}$) is used in the improved $k-\omega-\varphi-\alpha$ model, we find the same phenomenon observed by Durbin [25] in the $k-\varepsilon-\overline{v^2}$ model that a value being suitable for wall-bounded flow is not suitable for free shear flow. From a pragmatic view, a function based on the distance from the closest wall boundary and the turbulent length scale was suggested by Durbin [25] as

$$C_{\varepsilon 1} = 1.3 + \frac{0.25}{1+[C_L d/(2L)]^8}\,. \tag{14}$$

Similarly, in the improved $k-\omega-\varphi-\alpha$ model, a functional coefficient $C_{\varepsilon 1}^*$ is constructed based on Equations (13) and (14) as

$$C_{\varepsilon 1}^* = C_{\varepsilon 2} - \kappa^2\sigma_\omega/\sqrt{\beta^*} - C_{\varepsilon 5} + \frac{C_{\varepsilon 5}}{1+[C_L d/(2L)]^8}\,. \tag{15}$$

This equation gives $C_{\varepsilon 1}^{*} = C_{\varepsilon 2} - \kappa^2 \sigma_\omega / \sqrt{\beta^*}$ in the attached boundary layers and reverts to $C_{\varepsilon 1}^{*} = C_{\varepsilon 2} - \kappa^2 \sigma_\omega / \sqrt{\beta^*} - C_{\varepsilon 5}$ far away from wall boundary.

Then the formula of γ is

$$\gamma = C_{\varepsilon 1}^{*} - 1. \tag{16}$$

2.5 Consideration of the cross-diffusion term

The cross-diffusion term establishes a relationship between the $k-\varepsilon$ and the $k-\omega$ models and plays an important role in $k-\omega$ models [13].

To improve the performance of $k-\omega$ models, several researchers have attempted to add cross-diffusion term directly into the ω equation. However, there are several different motivated treatments for this term and all of them have achieved some degree of success. Among them, some researchers considered that the cross-diffusion term should be only activated when it is positive and this term should be suppressed close to solid boundaries for wall-bounded flow [13, 18, 26]. A typical form as listed in Equation (10) is

$$C_D = \max\left(\sigma_d \frac{\rho}{\omega} \frac{\partial k}{\partial x_j} \frac{\partial \omega}{\partial x_j}, 0.0 \right). \tag{17a}$$

However, others considered that the cross-diffusion term is important even though it is negative. They also regarded that the inclusion of the viscous cross-diffusion term is essential for wall-bounded flow in order to maintain the near-wall balance of the ω equation [27, 28]. Consequently, the cross-diffusion term takes the form as

$$C_D = \frac{\sigma_d}{k} \left(\mu + \mu_t \sigma_\omega \right) \frac{\partial k}{\partial x_j} \frac{\partial \omega}{\partial x_j}. \tag{17b}$$

In the famous SST $k-\omega$ model [22], a 'blending function', F_1 is introduced into the cross-diffusion term. The 'blending function' causes the SST $k-\omega$ model

preserving the desirable features of the $k-\omega$ model over a large portion of the boundary layer, but ensuring the free-stream independence of the $k-\varepsilon$ model elsewhere. This thinking is also used by Hallsten and Annti [29]. The cross-diffusion term they used is

$$C_D = 2(1-F_1)\frac{\rho\sigma_\omega}{\omega}\frac{\partial k}{\partial x_j}\frac{\partial \omega}{\partial x_j}. \tag{17c}$$

In the original $k-\omega-\varphi-\alpha$ model, the cross-diffusion term (Equation (6)) is divided into two parts. In the near wall region, the same treatment as the Wilcox's $k-\omega$ model is adopted, namely, the cross-diffusion term is contributed only when it is positive. In other regions, the cross-diffusion term holds the same formulation transformed from the BL$-\overline{v^2}/k$ model directly (regardless of positive or negative values). This treatment in the original $k-\omega-\varphi-\alpha$ model does not induce serious problem for flows with moderate and high turbulent intensity. However, our experiences showed that in the cases with very low turbulent intensity, this term may induce numerical difficulty (see Section 4.5).

In the improved $k-\omega-\varphi-\alpha$ model, the cross-diffusion term keeps the same form of the Wilcox's $k-\omega$ model, i.e. Equation (17(a)). The major reason is that this treatment not only have advantageous to stability of the model (see Section 4.5), but also can yield good predictions in the outer range of the boundary layer. It should be noted that the coefficient σ_d is retuned to reach good performance of the model.

2.6 Definitions of the turbulent scales

The definitions of the turbulent scales (length and time) used in turbulence models based on elliptic relaxation and elliptic blending are generally one of the Equations (18a) and (18b)

$$\begin{cases} L = C_L \max\left[\dfrac{\sqrt{k}}{\beta^*\omega}, C_\eta \dfrac{\nu^{3/4}}{\left(\beta^* k\omega\right)^{1/4}}\right] \\ T = \max\left[\dfrac{1}{\beta^*\omega}, C_T \dfrac{\nu^{1/2}}{\left(\beta^* k\omega\right)^{1/2}}\right] \end{cases}, \tag{18a}$$

$$\begin{cases} L = C_L \sqrt{\dfrac{k}{\left(\beta^*\omega\right)^2} + C_\eta^2 \dfrac{\nu^{3/2}}{\left(\beta^* k\omega\right)^{1/2}}} \\ T = \sqrt{\dfrac{1}{\left(\beta^*\omega\right)^2} + C_T^2 \dfrac{\nu}{\beta^* k\omega}} \end{cases}, \tag{18b}$$

where $\varepsilon = \beta^* k\omega$ has been used. It can be seen that all turbulent scales are limited by Kolmogorov scales to represent low-Reynolds-number effects in near wall region. Although the ways of switching into Kolmogorov scale are different between these two definitions (a function 'max' is used in Equation (18a) while a quadratic mean is used in Equation (18b)), the results obtained from them are similarly good.

To prevent over-prediction of turbulence near the stagnation point, an upper bound for the turbulent time scale is proposed by Durbin [30] as

$$T_{\lim} = \frac{\zeta}{\sqrt{3} C_\mu \varphi S}, \tag{19}$$

where ζ is an empirical constant which is less than one and should be calibrated according to the dimension (2D, axisymmetric or 3D) of the flow.

In present model, the turbulent scales are determined by using Equation (18a). Just as the $\mathrm{BL}-\overline{v^2}/k$ model, the limiter for the turbulent time scale is only utilised in the formulation of the turbulent viscosity (not in the φ equation). Namely, Equation (3) has not any change and the turbulent viscosity is

$$\mu_t = C_\mu \rho \varphi k \min(T, T_{\lim}). \tag{20}$$

2.7 Damping functions

Commonly, 'damping functions' are needed to be introduced into the $k-\varepsilon$ and $k-\omega$ models to correct the low-Reynolds-number (LRN) effects. For example, in the LRN Wilcox's $k-\omega$ model[13,18], there are three 'damping functions' which are individually used to damp the turbulent viscosity, the dissipation rate term in the k equation and the production term in the ω equation, in the LRN region. The 'damping functions' are

$$\begin{cases} f_\mu = \left[\beta_0/3 + \mathrm{Re}_t/6\right] \Big/ \left[1 + \mathrm{Re}_t/6\right] \\ f_k = \left[\beta_0/0.27 + (\mathrm{Re}_t/8)^4\right] \Big/ \left[1 + (\mathrm{Re}_t/8)^4\right] \\ f_\omega = \left(1/9 + \mathrm{Re}_t/2.61\right) \Big/ \left(1 + \mathrm{Re}_t/2.61\right) / f_\mu \end{cases}, \tag{21}$$

with $\mathrm{Re}_t = \rho k/(\mu\omega)$.

In the present model, the turbulent viscosity has been damped naturally when it is calculated by Equation (20) so that the 'damping function' f_μ for the turbulent viscosity is not needed. Actually, this characteristic is maintained for the series of $\overline{v^2}-f$ models. However, the 'damping function' f_k is needed. As illustrated in the original $k-\omega-\varphi-\alpha$ model [1], damping the dissipation rate term in the k equation can increase k in the near wall region thus predicting more accurate k profile. The 'damping function' f_ω, which is related to f_μ in the LRN $k-\omega$ model, can not be used directly just as Equation (21) because f_μ is not included in present model. However, an analogy function can be constructed. The 'damping functions' utilized finally in the present model are

$$f_k = \left[\beta_0/0.27 + (\mathrm{Re}_t/8)^4\right] \Big/ \left[1 + (\mathrm{Re}_t/8)^4\right], \tag{22}$$

$$f_\omega = \left[2.0 + \mathrm{Re}_t/2.61\right] \Big/ \left[1 + \mathrm{Re}_t/2.61\right]. \tag{23}$$

Consequently, the second term on the right-hand side of Equation (9) and the first term on the right-hand side of Equation (10) become as $f_k\rho\beta^* k\omega$ and $f_\omega\gamma\dfrac{\omega}{k}G_k$, respectively.

2.8 Limitation of the production of k

As previously mentioned in Section 2.6, introducing the upper bound of the turbulent time scale into the definition of the turbulent viscosity can prevent over-prediction of turbulence near the stagnation point. Beyond that, the over-prediction of the turbulence near the stagnation point can be alleviated by limiting the production of *k*. One of the effective methods is the correction of Kato and Launder [31], in which the production of *k* is computed by

$$G_k = \mu_t S\Omega \,, \tag{24}$$

rather than the conventional formula of

$$G_k = \mu_t S^2 \,. \tag{25}$$

However, considering the purpose of introducing Equation (24) is to limit the production of *k* in the region near the stagnation point, and that Equation (25) comes from the modelling process of the *k* equation and it seems to have better physical meaning than Equation (24) for general flow, a blending formulation of G_k, in which the blending function F_1 as the same used in the SST $k-\omega$ model, can be constructed. Namely, Equation (24) is only used in the near wall region and Equation (25) is used elsewhere. The final form of G_k reads

$$G_k = \mu_t S\left[F_1\Omega + (1-F_1)S\right]. \tag{26}$$

In present model, production of *k* is calculated using Equation (26). It should be noted that this modification has nearly no effect on the channel flow and the step flow, but it is a little inspiring that the results computed by Equation (26) is slightly better than Equation (24) and Equation (25) in the impinging jet flow (see Section 4.3).

2.9 Other considerations of the model

The final form of the improved $k-\omega-\varphi-\alpha$ model consists of Equations (9) and (10) with some modifications, together with Equations (3) and (4). There are a lot of model constants to be determined. Most of them are extracted directly from the Wilcox's $k-\omega$ model, the original $k-\omega-\varphi-\alpha$ model and the BL$-\overline{v^2}/k$ model, while others (as little as possible) should be modified or re-calibrated. 'Trial-and-error' efforts are made throughout this research. Appropriate values are assigned to ensure good (sometimes balanced) model performance to be kept for different flows.

The constant $C_{\varepsilon 2}$ is modified to be consistent with the β_0. Using the same values of $\beta_0 = 0.0708$ and $\beta^* = 0.09$ in the Wilcox's $k-\omega$ model, together with the consideration of $C^*_{\varepsilon 2} = C_{\varepsilon 2}$ and $\beta_0/\beta^* = C_{\varepsilon 2} - 1$ in the log-layer, $C_{\varepsilon 2} = 1.787$ can be obtained.

In present model, there are only six constants left (i.e. C_μ, $C_{\varepsilon 4}$, C_η, σ_d, $C_{\varepsilon 5}$ and ζ) need to be re-calibrated. Considering the fact that the importance of each parameter is different for specific flow, we used three kinds of typical flow to determine the parameter values (as shown in Table 1). Specifically, at first, the 2D fully developed channel flow (consider overall the velocity, turbulent kinetic energy and the turbulent viscosity) was used to determine C_μ, $C_{\varepsilon 4}$, C_η and σ_d. Then the 2D free jet flow (refer to the spreading rate) was used to determine $C_{\varepsilon 5}$. Finally, the 2D impinging jet flow (refer to the *Nu* at the stagnation point) was used to determine ζ.

For sake of clarity, the complete equations and constants of the improved $k-\omega-\varphi-\alpha$ model are recalled in Appendix A.

2.10 Energy equation

For incompressible flow, the governing equation of the energy can be simplified to the mean temperature equation. After using the Boussinesq approximation, the unknown eddy diffusivity of heat can be modelled by defining a turbulent Prandtl number, Pr_t. The governing equation of the mean temperature (θ) can be expressed as

$$\frac{\partial \rho\theta}{\partial t}+\frac{\partial}{\partial x_i}\left(\rho u_i\theta\right)=\frac{\partial}{\partial x_j}\left[\left(\frac{\mu}{\mathrm{Pr}}+\frac{\mu_t}{\mathrm{Pr}_t}\right)\frac{\partial\theta}{\partial x_j}\right], \tag{27}$$

where $\mathrm{Pr}=c_p\mu/k$ represents the molecular Prandtl number.

The turbulent Prandtl number Pr_t depends on several factors, e.g., the molecular Prandtl number (Pr) of the fluid, the viscosity of the fluid, and the Reynolds number of the flow [32]. There are substantial DNS and experimental data on the Pr_t. Based on the shape of the temperature in the log-layer of the boundary layer, the Pr_t can be assumed to be constant. However, there are no universal values of Pr_t, even in the simple wall shear flows. For example, for air flow with the molecular Prandtl number $\mathrm{Pr}=0.71$, the Pr_t ranges between 0.73 and 0.92 [32].

The DNS data for fully developed channel flow indicate $\mathrm{Pr}_t\approx 0.7$ at the centre of the channel with a non-monotonic increase to 1.2 at the wall. According to this, Kays and Crawford [33] proposed a formula for the Pr_t as

$$\mathrm{Pr}_t=\frac{1}{0.5882+0.228\left(\nu_t/\nu\right)-0.0441\left(\nu_t/\nu\right)^2\left[1-\exp\left(-5.165\nu/\nu_t\right)\right]}. \tag{28}$$

This formula yields a value of 1.7 at the wall and decreases asymptotically to a value of 0.85 far from the wall.

Although the Kays and Crawford formula (Equation (28)) provides a better shape for the Pr_t in boundary layer, it does not always yield better heat transfer predictions. For example, Durbin [34] simulated the flow and heat transfer in a 2D channel and in boundary layers adopting the Kays and Crawford formula and a constant

value of 0.9 together with the $k-\varepsilon-\overline{v^2}$ turbulence model. The results indicated that the constant Pr_t value yields a better agreement with experiments. Behnia et al. [35] used the $k-\varepsilon-\overline{v^2}$ model to compute the heat transfer in an axisymmetric turbulent jet impinging on a flat plate adopting the Kays and Crawford formula and the widely used constant values of 0.73, 0.85 and 0.92 in literatures. Park and Sung [36] used the $k-\varepsilon-f_\mu$ model developed by themselves to simulate the same problem adopting the Kays and Crawford formula and the constant values of 0.8 and 0.9. Their results indicate a common phenomenon that the local Nusselt number is not very sensitive to the Pr_t. Compared with available experimental data, it can be found that some values of Pr_t yield better results in the stagnation region, while others yield better predictions elsewhere. Therefore, it is difficult to say which value of Pr_t is better. For the improved $k-\omega-\varphi-\alpha$ model, the effect of Pr_t on the heat transfer will be tested in this study.

For sake of clarity, the mean temperature equation used in present study and the Kays and Crawford formula are recalled in Appendix B.

3 Solution procedure

It has been shown that the original $k-\omega-\varphi-\alpha$ model can yield a little better result in the 2D fully developed channel flow and comparable result in the separated flow than the $\mathrm{BL}-\overline{v^2}/k$ model. Moreover, the original $k-\omega-\varphi-\alpha$ model has better numerical stability and less sensibility to initial conditions [1]. Consequently, the original $k-\omega-\varphi-\alpha$ model is used to comparatively display the ability and the superiority of the improved $k-\omega-\varphi-\alpha$ model. For the purpose of reference, the popular SST $k-\omega$ model [22] is also considered.

3.1 Numerical method

The improved $k-\omega-\varphi-\alpha$ model and the original $k-\omega-\varphi-\alpha$ model are both implemented in the FLUENT CFD code using the User-Defined Function (UDF) functionality. The SST $k-\omega$ model is an inner-coded turbulence model in FLUENT and so it can be used directly.

The pressure-based segregated algorithm is used to solve the governing equations. The convection terms in the momentum and turbulence equations are all discretized by the second order upwind scheme. The least squares cell-based method is adopted to evaluate the gradients and derivatives. The velocity-pressure coupling process is dealt with by a combination of the SIMPLEC algorithm and the Coupled algorithm. Namely, at the early stage of iteration, the SIMPLEC algorithm, which is more stable, is used. After an appropriate flow field (not converged) being constructed, the iteration is switched to use the Coupled algorithm, which can promote the solution convergence. Because of the nonlinearity of the equation set being solved, the under-relaxation of variables is necessary to control the change of variables produced during each iteration. In general, the under-relaxation factors are problem and model dependent. In this study, the default under-relaxation factors are adopted for the pressure and velocities. For variables in the turbulence model, under-relaxation factors are set to be different values dependent on the complexity of the flow, for example, 0.8 for the fully developed channel flow and the backward-facing step flow, and smaller value for the impinging jet flow.

It should be noted that, for incompressible flow with constant thermal properties, the mean temperature equation (Equation (27)) is uncoupled with the fluid flow so that it can be solved independently. For each case in this study, the mean temperature equation is turned off firstly, then the isothermal fluid flow is solved and a fully

converged solution is obtained, finally the mean temperature equation is turned on and the iteration continues until the mean temperature has been convergent.

3.2 Boundary conditions on solid wall

The no-slip condition is used on solid walls, namely, $u_i = 0$, $k = 0$, $\varphi = 0$, $\alpha = 0$. For ω in the SST $k-\omega$ model, $\omega_w = 6\nu/(\beta_1 y_1^2)$ is used with y_1 representing the distance from the wall to the centre of the first cell adjacent to the wall. For ω both in the improved $k-\omega-\varphi-\alpha$ model and the original $k-\omega-\varphi-\alpha$ model, because the molecular diffusion has been halved, $\omega_w = 3\nu/(\beta_0 y_1^2)$ is used [1]. In all cases, the condition of $y^+ < 1$ is always ensured at the first grid point adjacent to the wall.

The thermal condition on solid wall may be specified to be adiabatic, with constant temperature or with constant heat flux, to consist with the related DNS and experimental results.

3.3 Initial conditions

The initial conditions not only have influence on the convergence speed, but also affect the convergence ability of the turbulence model. Although the initial conditions are generally empirical, some practical approaches can be suggested. As noted by Yang et al. [1], the value of zero for the initial flow velocity and a relatively larger initial value of ω are suggested to ensure the solution to be more stable. Additionally, initial values of $\varphi = 0.5$ and $\alpha = 1.0$ are appropriate and recommended for general problems. For the SST $k-\omega$ model, the default values in the FLUENT code are adopted.

4 Results and discussion

The abilities of the improved $k-\omega-\varphi-\alpha$ model for predicting the fluid flow and the heat transfer are evaluated and compared with the original $k-\omega-\varphi-\alpha$ model and the

Menter's SST $k-\omega$ model for three typical test cases: the 2D fully developed turbulent channel flow, the 2D backward-facing step flow and the 2D impinging jet flow. It should be noted that the LRN correction (similar to Equation (21)), which usually has strong influence on the behaviour of the turbulence model, is included in the SST $k-\omega$ model because similar correction is used both in the improved $k-\omega-\varphi-\alpha$ model and the original $k-\omega-\varphi-\alpha$ model.

4.1 Fully developed turbulent channel flow

Because there are many published available DNS data in literatures, the fully developed turbulent channel flow has been a widely used case for scrutinising the near-wall behaviours of turbulence models. In this study, we select four cases with different friction Reynolds number, Re_τ (550, 1000, 2000 and 5200), as the same used in our previous paper [1], to validate the performance of the improved $k-\omega-\varphi-\alpha$ model for fluid flow. The adopted DNS data, provided by Lee and Moser [37], are available online at http://turbulence.ices.utexas.edu. The results computed using the original $k-\omega-\varphi-\alpha$ model and the SST $k-\omega$ model are also included for comparison, although they have been compared in detail by Yang et al. [1].

The normalized mean streamwise velocity ($u^+ = u/u_\tau$) profiles are compared in Figure 2. It can be seen that the velocity profiles computed form the improved $k-\omega-\varphi-\alpha$ model and the original $k-\omega-\varphi-\alpha$ model are very similar and both of them yield predictions in excellent agreement with the DNS data. Apparently, the SST $k-\omega$ model under-predicts the velocity both in the buffer layer and the defect layer in all cases. Scrutinizing the buffer layer ($5 < y^+ < 30$), it can be found that the velocities computed using the improved $k-\omega-\varphi-\alpha$ model and the original $k-\omega-\varphi-\alpha$ model are almost indistinguishable for all Re_τ cases. This indicates that re-

movement of the '*E*' term does not reduce the accuracy of the improved $k-\omega-\varphi-\alpha$ model in buffer layer of the channel flow. The reason may be that the absence of the 'E' term can be remedied by re-adjusting other terms in the $k-\omega$ system.

The comparisons of the normalized turbulent kinetic energy ($k^+ = k/u_\tau^2$) profiles are shown in Figure 3. It is obvious that the SST $k-\omega$ model under-predicts the k^+ in all cases. At lower Re_τ case (e.g. $\mathrm{Re}_\tau = 550$), the improved $k-\omega-\varphi-\alpha$ model over-predicts the peak value of k^+, while the peak value of k^+ from the original $k-\omega-\varphi-\alpha$ model is comparable with the DNS result. At higher Re_τ case (e.g. $\mathrm{Re}_\tau = 5200$), both of the improved $k-\omega-\varphi-\alpha$ model and the original $k-\omega-\varphi-\alpha$ model under-predict the peak value of k^+.

The normalized Reynolds shear stress ($-\overline{u'v'}^+ = -\overline{u'v'}/u_\tau^2$) profiles are shown in Figure 4. Apparently, in all Re_τ cases, all turbulence models yield good Reynolds shear stress profiles compared to the DNS data. The Reynolds shear stress profiles decrease linearly towards the centre of the channel and are almost independent on turbulence models. This is not surprised because the total shear stress of the flow is controlled intrinsically by fluid dynamics, rather than turbulence models. From the fluid dynamic theory, it can be derived that the total shear stress decreases linearly from τ_w (shear stress at the wall) to zero (at the centre of the channel) [38], namely

$$\tau(y) = \rho\nu\frac{d\overline{u}}{dy} - \rho\overline{u'v'} = \tau_w\left(1-\frac{y}{\delta}\right) \tag{29}$$

In the region far away from the wall, the viscous shear stress ($\rho\nu d\overline{u}/dy$) is negligible, so that Equation (29) can be simplified to be

$$-\rho\overline{u'v'} = \tau_w\left(1-\frac{y}{\delta}\right) \tag{30}$$

This means the Reynolds shear stress ($-\rho\overline{u'v'}$) decreases linearly with respect to y, the distance from the wall.

Based on the Boussinesq hypothesis, which is employed by all turbulence models in this study, in channel flow the relationship between the Reynolds shear stress to the mean velocity gradient is

$$-\rho\overline{u'v'} = \rho\nu_t \frac{d\overline{u}}{dy} \tag{31}$$

Because Reynolds shear stress is independent on turbulence model (Figure 4), Equation (31) indicates that the better turbulent viscosity profile is predicted by the turbulence model, the better velocity gradient will be yielded, and further the better velocity profile can be obtained, and vice versa. Figure 5 shows the normalized turbulent viscosity ($\nu^+ = \nu_t / \nu$) profiles. The SST $k-\omega$ model over-predicts dramatically the turbulent viscosity in the central region of the channel, thus under-predicting the velocity profile (refer to Figure 2). Both of the improved $k-\omega-\varphi-\alpha$ model and the original $k-\omega-\varphi-\alpha$ model yield more reasonable turbulent viscosity profiles. The most important feature is they reduce the turbulent viscosity in the central region of the channel, thus leading to improvement of the velocity profile. Glancing at Figure 5, one can find that the turbulent viscosity profiles yielded by the improved $k-\omega-\varphi-\alpha$ model and the original $k-\omega-\varphi-\alpha$ model are similar in the near wall region, but are different in the central region of the channel. An interesting phenomenon is that the velocity profiles predicted by these two turbulence models have only slight difference despite the turbulent viscosity profiles are obviously different. It is not surprised because the velocity is an integral quantity. It is easy to understand from Equation (31) that the turbulent viscosity near the wall (but outer of the viscous sub-layer) has significant effect on the velocity profile. In this region, the Reynolds shear stress is large, so that small difference of turbulent viscosity will lead to large variation of velocity gradient, thus resulting in significantly different velocity profiles. On the contrary, in the central

region of the channel, because the Reynolds shear stress is small, the change of velocity gradient is not so large even though the difference of the turbulent viscosity is distinct.

From Figure 2 and Figure 5, the difference both in the velocity and the turbulent viscosity profiles computed using the improved $k-\omega-\varphi-\alpha$ model and the original $k-\omega-\varphi-\alpha$ model can be distinctly observed in the log-layer and the defect layer. The reason is that different turbulence models usually have different performances. The terms included in the equations of turbulence model, the selection of the model parameters, the definition of the turbulent viscosity, and so on, will affect the model performance. Based on the fact that the selection of some of the model parameters are entirely experiential, it is difficult to find a set of parameters which are superior to others for all kinds of flow. In practice, one can only try to ensure good (sometimes balanced) model performance to be kept for different flows as far as possible. For instance, from Figure 2 and Figure 5, it can be observed that for low Re_τ cases ($\mathrm{Re}_\tau = 550,1000$), the results from the original $k-\omega-\varphi-\alpha$ model are better. On the other hand, for high Re_τ case ($\mathrm{Re}_\tau = 5200$), the results from the improved $k-\omega-\varphi-\alpha$ model are better. However, it should be emphasized that the difference is not significant. We can decrease the σ_d and $C_{\varepsilon 4}$ synchronously to improve the results at low Re_τ cases, but the results at high Re_τ cases will become poor. Therefore, the final decision of the parameters is to insure reasonable results (the error is within a reasonable range) for all Re_τ cases.

4.2 2D backward-facing step flow

The backward-facing step flow (abbreviated as step flow later), which has simple geometry but abundant flow phenomena, such as flow separation, recirculation, reattachment and flow re-development, is a test case being selected most frequently for turbulence model validation. The experiment of Jovic and Drive [39] is most frequently

used in benchmarking the performance of turbulence models for separated flow [1, 18, 25, 27]. In their experiment, the expansion ratio of the test section is 1.2. The Reynolds number, Re_H, based on the step height, *H*, and mean bulk velocity of the inlet channel, U_b, is 5000. A companion DNS research was performed by Le et al. [40] with a slightly different Re_H of 5100 and good agreements were achieved.

The size of the computational domain, the boundary conditions and the computational meshes adopted can be found in Yang et al. [1]. For the convenience of discussion, the sketch of the geometry and the relevant boundary conditions of the step flow model are shown in Figure 6.

The skin friction coefficient C_f (defined as $C_f = 2\tau_w/(\rho U_b^2)$) along the bottom wall is usually used to justify the ability of turbulence model for this type flow. Figure 7 shows the comparisons of the computed C_f using different turbulence models against the experimental measurements of Jovic and Drive [39]. It can be found that, as the whole, the improved $k-\omega-\varphi-\alpha$ model and the original $k-\omega-\varphi-\alpha$ model can yield better C_f. They can yield larger negative C_f in the recirculation region and larger positive C_f in the re-development region than the SST $k-\omega$ model. Another quantity frequently used to verify the ability of the turbulence model is the location of the reattachment point. The improved $k-\omega-\varphi-\alpha$ model, the original $k-\omega-\varphi-\alpha$ model and the SST $k-\omega$ model give $6.49H$, $6.56H$ and $7.0H$, respectively. Compared with the experimental result of $6.0H$ and DNS result of $6.23H$, the improved $k-\omega-\varphi-\alpha$ model predicts the best.

Figure 8 shows the pressure coefficient ($C_p = 2(p-p_{ref})/(\rho U_b^2)$) distribution along the bottom wall. It can be seen that all turbulence models yield good results. The result predicted by the improved $k-\omega-\varphi-\alpha$ model is better in the region from the concave corner to the reattachment point.

Figure 9 shows the non-dimensional streamwise velocity (u/U_b) profiles computed using three turbulence models and extracted from the correspondingly experimental results of Jovic and Drive [39] at locations of $-3.12H$, $4H$, $6H$, $10H$, $15H$ and $19H$. Generally speaking, all three turbulence models can yield good results in the near wall region compared to the experiment. The difference between the results computed from the improved $k-\omega-\varphi-\alpha$ model and the original $k-\omega-\varphi-\alpha$ model is very slight. It should be noted that the SST $k-\omega$ model predicts smaller velocity in the central region of the channel than other two models. This phenomenon accords with the fact that the SST $k-\omega$ model under-predicts the velocity in the central region of the channel flow (refer to Figure 2 in Section 4.1).

4.3 2D turbulent impinging jet flow

Turbulent impinging jet is a widely studied flow configuration because its fundamental and industrial importance. Turbulent impinging jet flow has several complex features (such as free shear, stagnation and high streamline curvature) which have been proved to be somewhat difficult to be predicted by turbulence models. Therefore, this flow is frequently chosen to be a validation case for new turbulence model. The impinging jet flow which has been paid more attention to covers plane impinging jet flow (2D) and circular impinging jet flow (axisymmetric or 3D). In this study, only the plane impinging jet is considered. Many experimental researches have been performed to measure the wall pressure, wall shear stress, velocity profiles and heat transfer coefficient [41-45]. This flow has also been investigated numerically by several researchers using RANS turbulence models [46, 47], LES [48, 49] and hybrid RANS-LES model [50], respectively. It has been shown that this flow is particularly challenging for RANS models [46], while the LES and the RANS-LES model can yield much better flow prediction than the RANS models.

The experimental results of the case with H/B = 4 and Re = 20000 (based on the width of the slot, B, and the mean velocity at inlet, V_0) measured by Ashforth-Frost et al. [42] and Zhe and Modi [43] are chosen to check the performance of the turbulence models. As a supplement, the experimental data of the case with H/B = 4 and Re = 18000 of Dogruoz et al. [45] are used for the comparison of the friction coefficient. The numerical model (geometry and boundary conditions) is accorded with the experimental setups of Ashforth-Frost et al. [42] and Zhe and Modi [43], and the numerical model used by Dutta et al. [46]. The geometry and the physical quantities are symmetric about the centreline of the jet inlet (slot), so that only one half of the geometry is considered. The computational domain consists of a rectangular box as shown in Figure 10. The height (H) and the length (L) of the domain are $H = 4B$ and $L = 50B$, respectively. It should be noted here that in the experiments of Ashforth-Frost et al. [42] and Zhe and Modi [43] and in the computational model of Kubacki et al. [50], the jet is semi-confined. However, it was found that, comparing to using full-confinement wall, using semi-confinement wall has only slight effects on the jet behaviour in the region near the stagnation point. Therefore, similar to Dutta et al. [46], a full-confinement wall is used in our simulation. The boundary conditions are also shown in Figure 10. The symmetry boundary condition is used at the centreline of the slot. On all walls, no-slip boundary condition is employed (refer to Section 3.2 for details). At the outlet, the pressure outlet condition (with constant static pressure) is adopted. At the inlet, the velocity profile, turbulent kinetic energy (k) and specific dissipation rate (ω) are specified as the same as Kubacki et al. [50], namely, $u = 0$, $v = -V_0\left[1-(2x/B)^{14}\right]$, $k = 1.5(IV_0)^2$, $\omega = k^{1/2}/(0.015B)$. The turbulent intensity at inlet is $I = 1.0\%$. In the improved $k-\omega-\varphi-\alpha$ model and the original $k-\omega-\varphi-\alpha$ model, the values of φ and α at inlet are also needed. However, there is no enough information for them in literatures. Considering the velocity is almost flat at inlet, that is to say the boundary layer is very thin, so that $\alpha = 1$ is a

reasonable selection. Based on the experimental conditions of Ashforth-Frost et al. [42] and Zhe and Modi [43], it could be believed that the turbulence at inlet is almost fully developed. Therefore, in present simulation, $\varphi = 0.4$ is used (φ ranging from 0 to 2/3 in 2D fully developed turbulent flow). The computational cells are non-uniformly distributed. They are refined in the region close to walls and in the shear layers of the jet. To ensure mesh independent solutions being obtained, a grid sensitive study is performed. The total number of computational cells finally used is 140,000.

The pressure distribution on the impingement wall is compared in Figure 11, in which the pressure has been normalized by the maximum pressure (denoted as $p_{\max}$, occurring at the stagnation point) in each case. It can be seen that in whole region the distributions of the pressure computed from all turbulence models are almost indistinguishable and they agree well with the experimental result of Ashforth-Frost et al. [42].

Figure 12 shows a comparison of the skin friction coefficient C_f (defined as $C_f = 2\tau_w/(\rho V_0^2)$) along the impingement wall. The experimental results measured by Dogruoz et al. [45] and Zhe and Modi [43] are both chosen for comparison. It is apparent that the results from Dogruoz et al. [45] and Zhe and Modi [43] are different significantly. It should be emphasized that C_f has strong dependence on the measurement technique. Dogruoz et al. [45] used two techniques, the Stanton gauge and the oil film, to measure the C_f in the same flow condition but much different results were yielded. It was proved that the oil film result is more accurate so that in Figure 12 the oil film result form Dogruoz et al. [45] is used. The authors believed that the large deviation between the experimental results of Dogruoz et al. [45] and Zhe and Modi [43] is resulting from the difference of the measurement technique, rather than different Re.

It can be seen that, in the region near the stagnation point ($x/B<2$), all three turbulence models predict identical C_f and they agree well with the measurements of Dogruoz et al. [45]. In the region of $2<x/B<8$, the results computed by the three turbulence models deviate from each other. Though the dip and the secondary maxima of the C_f are predicted by all three models, those computed by the original $k-\omega-\varphi-\alpha$ model and the SST $k-\omega$ model are delayed markedly. On the contrary, the improved $k-\omega-\varphi-\alpha$ model predicts the dip and the secondary maxima slightly earlier and whose result is the best one. At large distance ($x/B>8$), the results yielded by all three models are close again.

The effect of the computing method for the production of k on C_f are also examined. The C_f computed by the improved $k-\omega-\varphi-\alpha$ model using Equation (24), (25) or (26) for the production of k is compared with experimental results in Figure 13. It is observed that in the region near the stagnation point and in the zone of fully developed wall jet, the computing method for the production of k have no effect on C_f. However, in the region of transition form laminar to turbulent, the effect is significant. Specifically, the result using Equation (24) is most close to the experimental result, while the one using Equation (25) is deviated greatly. The result using Equation (26) is in the middle.

Figure 14 shows comparisons of the mean streamwise velocity profiles (normalized by V_0) predicted by all three turbulence models with the available experimental data of Ashforth-Frost et al. [42] and Zhe and Modi [43]) at different vertical planes. It can be observed that from the $x/B=1$ plane to the $x/B=3$ plane (Figure 14(a)-14(c)), the velocity profiles in the region near the impingement wall ($y/B<3$) predicted by all three turbulence models are almost identical and they agree fairly well with the measurements of Ashforth-Frost et al. [42] and Zhe and Modi [43]. This characteristic can explain well why these three models can predict identical C_f in

the region near the stagnation point (see Figure 12). At the $x/B=5$ plane (Figure 14(d)), the original $k-\omega-\varphi-\alpha$ model and the SST $k-\omega$ model predict identical velocity profiles in the region near impingement plate yet. The improved $k-\omega-\varphi-\alpha$ model predicts larger velocity gradient near the impingement wall, further leading to larger friction force. This phenomenon just explains why the improved $k-\omega-\varphi-\alpha$ model yields larger C_f than the original $k-\omega-\varphi-\alpha$ model and the SST $k-\omega$ model at the $x/B=5$ plane (see Figure 12).

4.4 Heat transfer

The convective heat transfer has tight relationship with the fluid flow, further the performances of the turbulence models. Two flow configurations, namely the 2D fully-developed channel flow and the 2D impinging jet flow, are used to verify the performance of the improved $k-\omega-\varphi-\alpha$ model for the convective heat transfer. Also, the results computed by the original $k-\omega-\varphi-\alpha$ model and the SST $k-\omega$ model are included for comparison.

For the 2D fully-developed channel flow, two cases with friction Reynolds number of $\mathrm{Re}_\tau=395$ and $\mathrm{Re}_\tau=1020$ are considered. The simulation of the fluid flow is the same as Section 4.1. In the convective heat transfer calculation, a uniform heat flux boundary condition is imposed on the channel wall. The molecular Prandtl number is set to be $\mathrm{Pr}=0.71$. The DNS data adopted for comparison can be obtained from the computation of Abe et al. [51].

Figure 15 shows the comparisons of the normalized temperature ($\theta^+=(\theta_w-\theta)\rho c_p u_\tau/h$) profiles computed using different turbulence models. The Kays and Crawford formula is utilised in all computations. It can be found that in the viscous sub-layer the turbulence models have no influence on the temperature. The SST $k-\omega$ model under-predicts the temperature in the buffer layer and the defect layer

significantly for both Re_τ cases. The improved $k-\omega-\varphi-\alpha$ model and the original $k-\omega-\varphi-\alpha$ model predict similar temperature profiles and they both agree well with the DNS data.

The effect of the turbulent Prandtl number, Pr_t, on the heat transfer behaviour of the improved $k-\omega-\varphi-\alpha$ model is also studied. Three widely used constant Pr_t values of 0.73, 0.85, 0.92 [35], and the Kays and Crawford formula (Equation (28)) are tested. Figure 16 shows the predictions of the normalized temperature profiles. It can be seen that in the viscous sub-layer, the temperature profile is insensitive to the Pr_t. However, outside of the viscous sub-layer, the temperature profile becomes dramatically sensitive to the Pr_t. When $\mathrm{Pr}_t = 0.73$ and $\mathrm{Pr}_t = 0.85$, the temperature is under-predicted for both Re_τ cases. $\mathrm{Pr}_t = 0.92$ gives better results, even though the temperature profiles in the buffer layer and the log-layer are slightly under-predicted. The temperature profile computed using the Kays and Crawford formula at $\mathrm{Re}_\tau = 1020$ has good agreement with the DNS data. At $\mathrm{Re}_\tau = 395$, the Kays and Crawford formula over-predicts slightly the temperature profile yet. On the whole, the constant value of 0.92 and the Kays and Crawford formula yield better results than other Pr_t values.

For the 2D impinging jet, the fluid flow computation is the same as in Section 4.3. The boundary conditions for the heat transfer calculation are also shown in Figure 10. At the inlet, a constant temperature ($\theta_{in} = 300\,\mathrm{K}$) boundary condition is specified. At the confinement wall, the adiabatic condition is adopted. At the impingement wall, there are two available choices, i.e. a constant temperature condition and a constant heat flux condition. Dutta et al. [46] studied the effect of the thermal boundary condition on the *Nu* distribution on the impingement wall and found that the constant temperature condition was able to predict better result comparing to the experimental data of Ashforth-Frost et al. [42]. The constant temperature boundary condition was also performed in the computations on the same configuration by Kubacki et al. [50].

However, this treatment is lake of physics because in the experiments of Ashforth-Frost et al. [42] it is clearly pointed out that a constant heat flux boundary condition was applied. Therefore, in this study the constant heat flux boundary condition is used. The working fluid is air, and the molecular Prandtl number is $\mathrm{Pr} = 0.71$.

Figure 17 shows the comparison of the *Nu* (defined as $Nu = qB/[k(\theta_{wall} - \theta_{in})]$) distribution on the impingement wall measured by Ashforth-Frost et al. [42] and those predicted by different turbulence models with the Kays and Crawford formula (Equation (28)). It can be seen that, on the whole impingement wall, the *Nu* distribution predicted by the improved $k-\omega-\varphi-\alpha$ model agrees fairly well with the experimental result, but those predicted by the original $k-\omega-\varphi-\alpha$ model and the SST $k-\omega$ model are not good. Moreover, at the stagnation point, the *Nu* predicted by both of the improved $k-\omega-\varphi-\alpha$ model and the original $k-\omega-\varphi-\alpha$ model agree excellently with the experimental measurements. However, the SST $k-\omega$ model under-predicts it. All turbulence models are able to predict the dip and the secondary peak of *Nu*, which are connected with the transition form laminar to turbulent, though the peak values are significantly different. The original $k-\omega-\varphi-\alpha$ model and the SST $k-\omega$ model delay the dip of *Nu* so much. An interesting phenomenon is that, in the region far away from the stagnation point (about $x/B>10$), all three turbulence models yield similar *Nu*.

Scrutinising some terms in the original $k-\omega-\varphi-\alpha$ model, we find that one of the reasons, which lead to transition delayed, is the '*E*' term. Figure 18 shows the comparison of the *Nu* distribution using the original $k-\omega-\varphi-\alpha$ model with and without the '*E*' term. It is apparent that when the '*E*' term is removed, the *Nu* distribution is improved significantly. This demonstrated that including the '*E*' term is detrimental, so that in the improved $k-\omega-\varphi-\alpha$ model this term is dropped out.

The effect of the computing method for the production of *k* on *Nu* are also examined. Figure 19 shows the comparison of the *Nu* computed by the improved

$k-\omega-\varphi-\alpha$ model using Equation (24), (25) and (26) for the production of k. It can be seen that in the regions near the stagnation point and in the fully developed wall jet, the computing method for the production of k have slight effect on *Nu*. However, in the transition region, the effect is significant. Specifically, the result using Equation (26) is between those using Equation (24) and Equation (25). It should be emphasized that Equation (24) yields the best C_f, but yields the worst *Nu* meanwhile. Taking into consideration that the measurement of C_f is more difficult than the measurement of *Nu*, that is the result of *Nu* is more reliable than that of C_f, the result of *Nu* should be used to estimate the performance of the methods. Among them, Equation (26) can yield a better result of *Nu* and strike a balance for C_f, so that we decide to use Equation (26) in the improved $k-\omega-\varphi-\alpha$ model.

To investigate the effect of the turbulent Prandtl number, Pr_t, on the Nusselt number (*Nu*), three constant Pr_t values of 0.73, 0.85, 0.92, together with the Kays and Crawford formula are tested using the improved $k-\omega-\varphi-\alpha$ model. The results shown in Figure 20 indicate that the *Nu* is not much sensitive to Pr_t in the region of $x/B<3$, even though the three constant Pr_t over-predict slightly the *Nu* at the stagnation point. On the whole, it is difficult to say which value of Pr_t can yield the best result because the result from the Kays and Crawford formula is better in the region near the stagnation point, but the result from $\mathrm{Pr}_t=0.73$ is better in the region downstream the transition. Taking into account their performances in the channel flow, in which the performance of $\mathrm{Pr}_t=0.73$ is the worst, the performance of the Kays and Crawford formula is better.

4.5 Stability of the model

A relatively serious problem for the original $k-\omega-\varphi-\alpha$ model is that it is difficult to obtain convergent solution in problems with very low turbulent intensity. As an

example, the impinging jet flow with very low turbulent intensity is considered. For inlet boundary conditions, except the turbulent intensity, which is set to be 0.1% just as in the simulation of Jaramillo et al. [52], other quantities are the same as those in Section 4.3. Keeping other coefficients to be unchanged, the under-relaxation factors for turbulence quantities (same factors are used for all turbulence quantities) are able to be adjusted. It is well known that the larger under-relaxation factor is permitted by the model, better stability the model has. It is found that, for the original $k-\omega-\varphi-\alpha$ model, even when the under-relaxation factor decrease to be 0.005, convergent solution can not be obtained yet. On the other hand, for the improved $k-\omega-\varphi-\alpha$ model, convergent solution can be obtained even when the under-relaxation factor is large to be 0.6.

The stability of the model can also be investigated using the same method in the study of Yang et al. [1]. A disturbance is introduced to a converged solution, and the effect of the disturbance on the subsequent solution behaviour is evaluated. For the sake of simplicity, only the impinging jet flow is considered. The computational meshes, the boundary conditions, the discrete schemes for governing equations and the under relaxation factors for pressure, momentum and other scalars are the same for all simulations using different turbulence models. In each case, the disturbance is only introduced to the turbulent kinetic energy (k) by changing it from the converged value to $2k_{in}$, $3k_{in}$, $4k_{in}$, $\cdots$ (k_{in} represents the area-weighted average value of k at inlet) in whole computational domain, and then the computation is continued. It is found that, for the improved $k-\omega-\varphi-\alpha$ model, the solution is able to converge until k becomes $30k_{in}$ (larger disturbance is not tested further), but for the original $k-\omega-\varphi-\alpha$ model the solution diverges when k becomes $4k_{in}$. This means that the improved $k-\omega-\varphi-\alpha$ model can bear much larger disturbance and has better stability.

Low stability of the original $k-\omega-\varphi-\alpha$ model results partly from the cross-diffusion term, C_D. The Wilcox's $k-\omega$ model and the Menter's SST $k-\omega$ model have enjoyed more successes among the $k-\omega$ models. One of the reasons is that these two models suppress successfully the cross-diffusion term close to solid boundaries for wall bounded flows[13]. However, in the original $k-\omega-\varphi-\alpha$ model, the cross-diffusion term can not be completely suppressed. This feature can be illustrated in Figure 1. Obviously, in the viscous sub-layer, large negative value of cross-diffusion term exists. For flow with low turbulent intensity (k and ω are both small), this problem will be more serious. Refer to Equation (6), k occurs in the denominator of the definition of C_D, thus smaller k resulting in larger negative value of C_D in the viscous sub-layer. Consequently, it is not surprised that the numerical difficulty may be encountered when the original $k-\omega-\varphi-\alpha$ model is used for flows with very low turbulent intensity. The improved $k-\omega-\varphi-\alpha$ model uses the same cross-diffusion term as the Wilcox's $k-\omega$ and the problem of stability coming from the cross-diffusion term can be successfully eliminated.

4.6 Computational efficiency of the model

The impinging jet flow is used to examine the computational efficiency of the improved $k-\omega-\varphi-\alpha$ model. Three cases with different number of computational cells are carried out. Based on same computer hardware and software, the time consume for 100 iterations in each case is recorded. The results are listed in Table 2. The results coming from the original $k-\omega-\varphi-\alpha$ model based on same conditions are included for comparison. It can be seen that the improved $k-\omega-\varphi-\alpha$ model always saves time in all cases. It is not surprised because the improved $k-\omega-\varphi-\alpha$ model drops out the 'E' term and the 'D_k' term, which include the second order derivatives of velocity and turbulent kinetic energy respectively and need to consume more computational time.

On the other hand, the maximum relaxation factors for turbulent quantities permitted by the improved $k-\omega-\varphi-\alpha$ model are commonly larger than those permitted by the original $k-\omega-\varphi-\alpha$ model because the former has better stability. Based on the fact that larger relaxation factor leading to convergence more quickly, the improved $k-\omega-\varphi-\alpha$ model can save time further.

Conclusions

An improved $k-\omega-\varphi-\alpha$ turbulence model is developed based on the elliptic blending concept and its capabilities are tested on the channel flow, the step flow and the impinging jet flow. Its performance on the convective heat transfer in the channel flow and the impinging jet flow is also investigated. The calculated results are validated using available DNS and experimental data, and the present model is also compared with the original $k-\omega-\varphi-\alpha$ model and the SST $k-\omega$ model. The results lead to the following conclusions:

(1) Comparing to the original $k-\omega-\varphi-\alpha$ model, the improved $k-\omega-\varphi-\alpha$ model has better numerical stability, higher computational efficiency and more concise form.

(2) Comparing to the original $k-\omega-\varphi-\alpha$ model, the improved $k-\omega-\varphi-\alpha$ model yields similar velocity and temperature profiles in the channel flow and close predictions for the fluid flow in the step flow. Both of them predict better results than the SST $k-\omega$ model.

(3) The improved $k-\omega-\varphi-\alpha$ model shows improved predictions for the fluid flow and heat transfer in the impinging jet flow compared with the original $k-\omega-\varphi-\alpha$ model and the SST $k-\omega$ model.

(4) Both of the turbulence model and the turbulent Prandtl number have significant effects on the convective heat transfer. The improved $k-\omega-\varphi-\alpha$ model combined with the Kays and Crawford formula can yield better results.

Acknowledgements

Support given by the National Natural Science Foundation of China (Project No. 51678364) and The Hong Kong Polytechnic University under grant No. G-YL41 is gratefully acknowledged.

Appendix A: Formulation of the improved *k–ω–φ–α* model

The equations of the improved $k-\omega-\varphi-\alpha$ model are briefly summarised below.

$$\frac{\partial \rho k}{\partial t}+\frac{\partial}{\partial x_i}\left(\rho u_i k\right)=G_k-\rho f_k \beta^* k\omega+\frac{\partial}{\partial x_j}\left[\left(\frac{\mu}{2}+\sigma_k \mu_t\right)\frac{\partial k}{\partial x_j}\right] \tag{A. 1}$$

$$\frac{\partial \rho \omega}{\partial t}+\frac{\partial}{\partial x_i}\left(\rho u_i \omega\right)=f_\omega \gamma \frac{\omega}{k}G_k-\rho\beta\omega^2+C_D+\frac{\partial}{\partial x_j}\left[\left(\frac{\mu}{2}+\sigma_\omega \mu_t\right)\frac{\partial \omega}{\partial x_j}\right] \tag{A. 2}$$

$$\frac{\partial \rho \varphi}{\partial t}+\frac{\partial}{\partial x_i}\left(\rho u_i \varphi\right)=\left(1-\alpha^p\right)\rho f_{wall}+\alpha^p \rho f_{\hom}-\frac{\varphi}{k}G_k+\frac{2}{k}\mu_t\sigma_k\frac{\partial \varphi}{\partial x_j}\frac{\partial k}{\partial x_j}+\frac{\partial}{\partial x_j}\left[\left(\frac{\mu}{2}+\sigma_\varphi \mu_t\right)\frac{\partial \varphi}{\partial x_j}\right] \tag{A. 3}$$

$$0=\frac{1-\alpha}{L^2}+\frac{\partial}{\partial x_j}\left(\frac{\partial \alpha}{\partial x_j}\right) \tag{A. 4}$$

$$\mu_t=C_\mu \rho \varphi k \min(T, T_{\lim}) \tag{A. 5}$$

$$G_k=\mu_t S\left[F_1\Omega+\left(1-F_1\right)S\right] \tag{A.6}$$

$$f_{wall}=-\frac{\beta^*\omega\varphi}{2} \tag{A.7}$$

$$f_{\hom}=-\frac{1}{T}\left(C_1-1+C_2\frac{G_k}{\rho\beta^* k\omega}\right)\left(\varphi-\frac{2}{3}\right) \tag{A.8}$$

$$F_1=\tanh(\Phi^4) \tag{A.9}$$

$$\Phi=\min\left[\max\left(\frac{\sqrt{k}}{0.09\omega y},\frac{500\mu}{\rho\omega y^2}\right),\frac{4\rho k\sigma_\omega}{D_\omega^+ y^2}\right] \tag{A.10}$$

$$D_\omega^+=\max\left(2\rho\sigma_\omega\frac{1}{\omega}\frac{\partial k}{\partial x_j}\frac{\partial \omega}{\partial x_j},10^{-10}\right) \tag{A.11}$$

$$f_k=\left[\beta_0/0.27+\left(\mathrm{Re}_t/8\right)^4\right]\Big/\left[1+\left(\mathrm{Re}_t/8\right)^4\right] \tag{A. 12}$$

$$f_\omega = \left[2.0 + \mathrm{Re}_t / 2.61\right] / \left[1 + \mathrm{Re}_t / 2.61\right] \tag{A.13}$$

$$\beta_0 = (C^*_{\varepsilon 2} - 1)\beta^* \tag{A. 14}$$

$$C^*_{\varepsilon 2} = C_{\varepsilon 2} + \alpha^p \left(C_{\varepsilon 4} - C_{\varepsilon 2}\right) \tanh\left[\max\left(\frac{D^t_k}{\beta^* k\omega}, 0\right)\right] \tag{A. 15}$$

$$D^t_k = \frac{\partial}{\partial x_j}\left(\frac{\mu_t \sigma_k}{\rho}\frac{\partial k}{\partial x_j}\right) \tag{A. 16}$$

$$\gamma = C^*_{\varepsilon 1} - 1 \tag{A. 17}$$

$$C^*_{\varepsilon 1} = C_{\varepsilon 2} - \kappa^2 \sigma_\omega / \sqrt{\beta^*} - C_{\varepsilon 5} + \frac{C_{\varepsilon 5}}{1 + [C_L d/(2L)]^8} \tag{A. 18}$$

$$C_D = \sigma_d \frac{\rho}{\omega} \max\left(\frac{\partial k}{\partial x_j}\frac{\partial \omega}{\partial x_j}, 0.0\right) \tag{A. 19}$$

$$\begin{cases} L = C_L \max\left[\dfrac{\sqrt{k}}{\beta^* \omega}, C_\eta \dfrac{\nu^{3/4}}{\left(\beta^* k\omega\right)^{1/4}}\right] \\ T = \max\left[\dfrac{1}{\beta^* \omega}, C_T \dfrac{\nu^{1/2}}{\left(\beta^* k\omega\right)^{1/2}}\right] \end{cases} \tag{A. 20}$$

$$T_{\lim} = \frac{\zeta}{\sqrt{3} C_\mu \varphi S} \tag{A. 21}$$

where $S = \sqrt{2 S_{ij} S_{ij}}$, $S_{ij} = \frac{1}{2}(u_{i,j} + u_{j,i})$, $\Omega = \sqrt{2\Omega_{ij}\Omega_{jk}}$, $\Omega_{ij} = \frac{1}{2}(u_{i,j} - u_{j,i})$, $\beta = \beta_0 f_\beta$, $f_\beta = 1$ and y is the distance to the nearest wall.

The model constants extracted (or computed) directly from the Wilcox's $k-\omega$ model, the BL$-\overline{v^2}/k$ model and the original $k-\omega-\varphi-\alpha$ model are listed in Table A.1 and those re-calibrated are listed in Table A.2.

Appendix B: The mean temperature equation used in present study

The mean temperature equation is

$$\frac{\partial \rho\theta}{\partial t} + \frac{\partial}{\partial x_i}\left(\rho u_i \theta\right) = \frac{\partial}{\partial x_j}\left[\left(\frac{\mu}{\mathrm{Pr}} + \frac{\mu_t}{\mathrm{Pr}_t}\right)\frac{\partial \theta}{\partial x_j}\right] \tag{B. 1}$$

with $\mathrm{Pr}_t = constant$ or

$$\mathrm{Pr}_t = \frac{1}{0.5882 + 0.228(\nu_t/\nu) - 0.0441(\nu_t/\nu)^2\left[1 - \exp\left(-5.165\nu/\nu_t\right)\right]} \quad \text{(B. 2)}$$

References

[1] X.L. Yang, L. Yang, Z.W. Huang, Y. Liu, Development of a k–ω–φ–α turbulence model based on elliptic blending and applications for near-wall and separated flows, Journal of Turbulence, 18 (2017) 36-60.

[2] P.R. Spalart, S. Deck, M.L. Shur, K.D. Squires, M.K. Strelets, A. Travin, A new version of detached-eddy simulation, resistant to ambiguous grid densities, Theoretical and Computational Fluid Dynamics, 20 (2006) 181-195.

[3] P. Quéméré, P. Sagaut, V. Couailler, A new multi-domain/multi-resolution method for large-eddy simulation, International Journal for Numerical Methods in Fluids, 36 (2001) 391-416.

[4] F.R. Menter, Y. Egorov, The scale-adaptive simulation method for unsteady turbulent flow predictions. Part 1: theory and model description, Flow, Turbulence and Combustion, 85 (2010) 113-138.

[5] P.A. Durbin, Near-wall turbulence closure modeling without damping functions, Theoretical and Computational Fluid Dynamics, 3 (1991) 1-13.

[6] F. Billard, D. Laurence, A robust k−ε−v^2/k elliptic blending turbulence model applied to near-wall, separated and buoyant flows, International Journal of Heat and Fluid Flow, 33 (2012) 45-58.

[7] W.P. Jones, B.E. Launder, The prediction of laminarization with a two-equation model of turbulence, International Journal of Heat and Mass Transfer, 15 (1972) 301-314.

[8] L. Thielen, K. Hanjalić, H. Jonker, R. Manceau, Predictions of flow and heat transfer in multiple impinging jets with an elliptic-blending second-moment closure, International Journal of Heat and Mass Transfer, 48 (2005) 1583-1598.

[9] F. Billard, A. Revell, T. Craft, Application of recently developed elliptic blending based models to separated flows, International Journal of Heat and Fluid Flow, 35 (2012) 141-151.

[10] ANSYS Inc, ANSYS Fluent V2F turbulence model manual, Southpointe, 2013.

[11] R.M. Jones, Advanced turbulence modeling for industrial flows, Agricultural and Mechanical College, Louisiana State University, 2003.

[12] O.Y. Taha, Formulation, implementation and testing of k-ω-v^2-f model in an asymmetric plane diffuser, Chalmers University of Technology, Göteborg, 2004.

[13] D.C. Wilcox, Turbulence modeling for CFD, DCW Industries Inc., La Canada, California, 2006.
[14] F.-S. Lien, G. Kalitzin, Computations of transonic flow with the v^2–f turbulence model, International Journal of Heat and Fluid Flow, 22 (2001) 53-61.
[15] M.R. Nazari, A. Sohankar, S. Malekzadeh, A. Alemrajabi, Reynolds-averaged Navier–Stokes simulations of unsteady separated flow using the k−ω−v^2−f model, Journal of Turbulence, 10 (2009) 1-13.
[16] M. Mirzaei, A. Sohankar, Numerical study of convective heat transfer and fluid flow around two side by side square cylinders using k−ω−v^2− f turbulence model, Heat and Mass Transfer, 49 (2013) 1755-1769.
[17] E. Khalaji, M.R. Nazari, Z. Seifi, 2D numerical simulation of impinging jet to the flat surface by k-ω-v^2-f turbulence model, Heat and Mass Transfer, 52 (2016) 127-140.
[18] D.C. Wilcox, Formulation of the k-ω turbulence model revisited, AIAA Journal, 46 (2008) 2823-2838.
[19] Z. Seifi, M.R. Nazari, E. Khalaji, 2D numerical simulation of impinging jet onto the concave surface by k-ω-v^2-f turbulence model, Heat and Mass Transfer, (2016).
[20] R. Manceau, K. Hanjalić, Elliptic blending model: A new near-wall Reynolds-stress turbulence closure, Physics of Fluids, 14 (2002) 744.
[21] F. Billard, Development of a robust elliptic-blending turbulence model for near-wall, separated and buoyang flows, School of Mechanical, Aerospace and Civil Engineering, The University of Manchester, Manchester, UK, 2011.
[22] F.R. Menter, Improved two equation k-ω turbulence models for aerodynamic flows, NASA Technical Memorandum, (1992).
[23] S. Jakirlic, K. Hanjalic, A new approach to modelling near-wall turbulence energy and stress dissipation, Journal of Fluid Mechanics, 459 (2002) 139-166.
[24] S. Jakirlić, J. Jovanović, R. Maduta, On near-wall treatment in (U)RANS-based closure models, Flow, Turbulence and Combustion, 91 (2013) 849-866.
[25] P.A. Durbin, Separated flow computations with the k-epsilon-v-squared model, AIAA Journal, 33 (1995) 659-664.
[26] J.C. Kok, Resolving the dependence on freestream values for the k-ω turbulence model, AIAA Journal, 38 (2000) 1292-1295.
[27] J. Bredberg, S.H. Peng, L. Davidson, An improved k−ω turbulence model applied to recirculating flows, International Journal of Heat and Fluid Flow, 23 (2002) 731-743.
[28] C.G. Speziale, R. Abid, E.C. Anderson, Critical evaluation of two-equation models for near-wall turbulence, AIAA Journal, 30 (1992) 324-331.
[29] A.K. Hellsten, New advanced k-ω turbulence model for high-lift aerodynamics, AIAA Journal, 43 (2005) 1857-1869.
[30] P.A. Durbin, On the k-3 stagnation point anomaly, International Journal of Heat and Fluid Flow, 17 (1996) 89-90.

[31] M. Kato, B.E. Launder, The modelling of turbulent flow around stationary and vibrating square cylinders, Ninth Symposium on "Turbulent Shear Flows" Kyoto, Japan, 1993, pp. 10-14-11-10-14-16.
[32] W.M. Kays, Turbulent Prandtl number—where are we?, Journal of Heat Transfer, 116 (1994) 284-295.
[33] W.M. Kays, M.E. Crawford, Convective heat and mass transfer, McGraw-Hill Education, New York, 1993.
[34] P.A. Durbin, Application of a near-wall turbulence model to boundary layers and heat transfer, International Journal of Heat and Fluid Flow, 14 (1993) 316-323.
[35] M. Behnia, S. Parneix, P.A. Durbin, Prediction of heat transfer in an axisymmetric turbulent jet impinging on a flat plate, International Journal of Heat and Mass Transfer, 41 (1998) 1845-1855.
[36] T.S. Park, H.J. Sung, Development of a near-wall turbulence model and application to jet impingement heat transfer, International Journal of Heat and Fluid Flow, 22 (2001) 10-18.
[37] M. Lee, R.D. Moser, Direct numerical simulation of turbulent channel flow up to Re_τ=5200, Journal of Fluid Mechanics, 774 (2015) 395-415.
[38] S.B. Pope, Turbulent Flows, Cambridge University Press, 2000.
[39] S. Jovic, D.M. Driver, Backward-facing step measurements at low Reynolds number Re_h=5000, NASA Technical Memorandum, 108807 (1994).
[40] H. Le, P. Moin, J. Kim, Direct numerical simulation of turbulent flow over a backward-facing step, Journal of Fluid Mechanics, 330 (1997) 349-374.
[41] C.V. Tu, D.H. Wood, Wall pressure and shear stress measurements beneath an impinging jet, Experimental Thermal and Fluid Science, 13 (1996) 364-373.
[42] S. Ashforth-Frost, K. Jambunathan, C.F. Whitney, Velocity and turbulence characteristics of a semiconfined orthogonally impinging slot jet, Experimental Thermal and Fluid Science, 14 (1997) 60-67.
[43] J. Zhe, V. Modi, Near wall measurements for a turbulent impinging slot jet (Data Bank Contribution), Journal of Fluids Engineering, 123 (2001) 112.
[44] V. Narayanan, J. Seyed-Yagoobi, R.H. Page, An experimental study of fluid mechanics and heat transfer in an impinging slot jet flow, International Journal of Heat and Mass Transfer, 47 (2004) 1827-1845.
[45] M.B. Dogruoz, A. Ortega, R.V. Westphal, Measurements of skin friction and heat transfer beneath an impinging slot jet, Experimental Thermal and Fluid Science, 60 (2015) 213-222.
[46] R. Dutta, A. Dewan, B. Srinivasan, Comparison of various integration to wall (ITW) RANS models for predicting turbulent slot jet impingement heat transfer, International Journal of Heat and Mass Transfer, 65 (2013) 750-764.

[47] A.M. Achari, M.K. Das, Application of various RANS based models towards predicting turbulent slot jet impingement, International Journal of Thermal Sciences, 98 (2015) 332-351.
[48] R. Dutta, B. Srinivasan, A. Dewan, LES of a turbulent slot impinging jet to predict fluid flow and heat transfer, Numerical Heat Transfer, Part A: Applications, 64 (2013) 759-776.
[49] R. Dutta, A. Dewan, B. Srinivasan, Large eddy simulation of turbulent slot jet impingement heat transfer at small nozzle-to-plate spacing, Heat Transfer Engineering, 37 (2016) 1242-1251.
[50] S. Kubacki, J. Rokicki, E. Dick, Hybrid RANS/LES computations of plane impinging jets with DES and PANS models, International Journal of Heat and Fluid Flow, 44 (2013) 596-609.
[51] H. Abe, H. Kawamura, Y. Matsuo, Surface heat-flux fluctuations in a turbulent channel flow up to Re_τ=1020 with Pr=0.025 and 0.71, International Journal of Heat and Fluid Flow, 25 (2004) 404-419.
[52] J.E. Jaramillo, F.X. Trias, A. Gorobets, C.D. Prez-Segarra, A. Oliva, DNS and RANS modelling of a turbulent plane impinging jet, International Journal of Heat and Mass Transfer, 55 (2012) 789-801.

Table captions

Table 1. The importance of the model parameters for different flow.

Table 2. The time consume for 100 iterations.

Table A.1. Model constants extracted (or computed) directly from the Wilcox's $k-\omega$ model, the $\mathrm{BL}-\overline{v^2}/k$ model and the original $k-\omega-\varphi-\alpha$ model.

Table A.2. Model constants re-calibrated in the improved $k-\omega-\varphi-\alpha$ model.

Figure captions

Figure 1. Comparison of the non-dimensional 'D_k' term and the cross-diffusion term 'C_D' for channel flow at $\mathrm{Re}_\tau = 1000$.

Figure 2. Comparisons of normalized mean streamwise velocity profiles. (a) $\mathrm{Re}_\tau = 550$; (b) $\mathrm{Re}_\tau = 1000$; (c) $\mathrm{Re}_\tau = 2000$; (d) $\mathrm{Re}_\tau = 5200$.

Figure 3. Comparisons of normalized turbulent kinetic energy profiles. (a) $\mathrm{Re}_\tau = 550$; (b) $\mathrm{Re}_\tau = 1000$; (c) $\mathrm{Re}_\tau = 2000$; (d) $\mathrm{Re}_\tau = 5200$.

Figure 4. Comparisons of normalized Reynolds stress. (a) $\mathrm{Re}_\tau = 550$; (b) $\mathrm{Re}_\tau = 1000$; (c) $\mathrm{Re}_\tau = 2000$; (d) $\mathrm{Re}_\tau = 5200$.

Figure 5. Comparisons of normalized turbulent viscosity profiles. (a) $\mathrm{Re}_\tau = 550$; (b) $\mathrm{Re}_\tau = 1000$; (c) $\mathrm{Re}_\tau = 2000$; (d) $\mathrm{Re}_\tau = 5200$.

Figure 6. Sketch of the geometry and boundary conditions of the step flow.

Figure 7. Skin friction coefficients on the bottom wall of the step flow.

Figure 8. Comparisons of pressure coefficient on the bottom wall of the step flow.

Figure 9. Velocity profiles at different locations of the step flow.

Figure 10. Sketch of the geometry and boundary conditions for the impinging jet flow.

Figure 11. Comparison of the pressure distribution on the impingement wall.

Figure 12. Comparison of the skin friction coefficient along the impingement wall.

Figure 13. Effect of the formula for the production of *k* on the skin friction coefficient.

Figure 14. Comparisons of the mean streamwise velocity profiles at different vertical planes. (a) $x/B = 1$; (b) $x/B = 2$; (c) $x/B = 3$; (d) $x/B = 5$.

Figure 15. Comparisons of the dimensionless mean temperature profiles computed by different turbulence models. (a) $\mathrm{Re}_\tau = 395$; (b) $\mathrm{Re}_\tau = 1020$.

Figure 16. Predictions of the dimensionless mean temperature profiles by the improved $k-\omega-\varphi-\alpha$ model with different Pr_t. (a) $\mathrm{Re}_\tau = 395$; (b) $\mathrm{Re}_\tau = 1020$.

Figure 17. Comparison of the Nusselt number distribution on the impingement wall.

Figure 18. Comparison of the Nusselt number computed using the original $k-\omega-\varphi-\alpha$ model with and without the '*E*' term.

Figure 19. Effect of the formula for the production of *k* on the Nusselt number distribution.

Figure 20. The effect of the turbulent Prandtl number on the Nusselt number.

Table 1.

Flow type	C_{μ}	$C_{\varepsilon 4}$	C_{η}	σ_d	$C_{\varepsilon 5}$	ζ
2D channel flow	√	√	√	√		
2D free jet flow	√	√	√	√	√	
2D impinging jet flow	√	√	√	√	√	√

Table 2.

	The number of Cells		
	140000	280000	640000
Improved $k-\omega-\varphi-\alpha$	47s	87s	732s
Original $k-\omega-\varphi-\alpha$	51s	98s	833s

Table A.1.

β^*	σ_k	σ_ω	κ	p	σ_φ	$C_{\varepsilon 2}$	C_1	C_2	C_T	C_L
0.09	0.6	0.5	0.41	4.0	1.0	1.787	1.7	0.9	6.0	0.164

Table A.2.

C_{μ}	$C_{\varepsilon 4}$	C_{η}	σ_d	$C_{\varepsilon 5}$	ζ
0.21	1.2	79	0.5	0.17	1.0

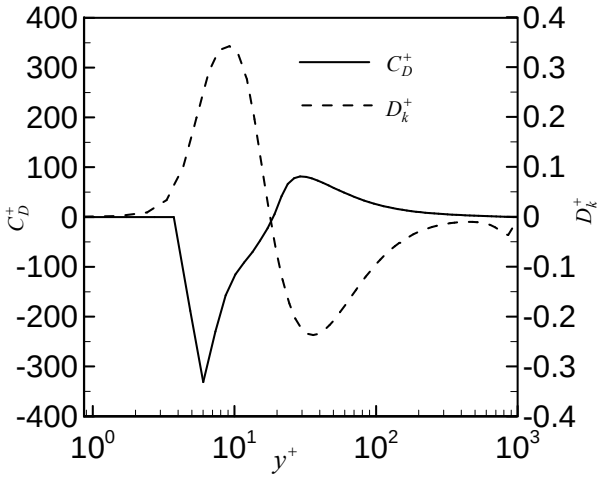
400
300
200
100
0
-100
-200
-300
-400
0.4
0.3
0.2
0.1
0
-0.1
-0.2
-0.3
-0.4
C_D^+
D_k^+
10^0
10^1
10^2
10^3
y^+

Figure 1.

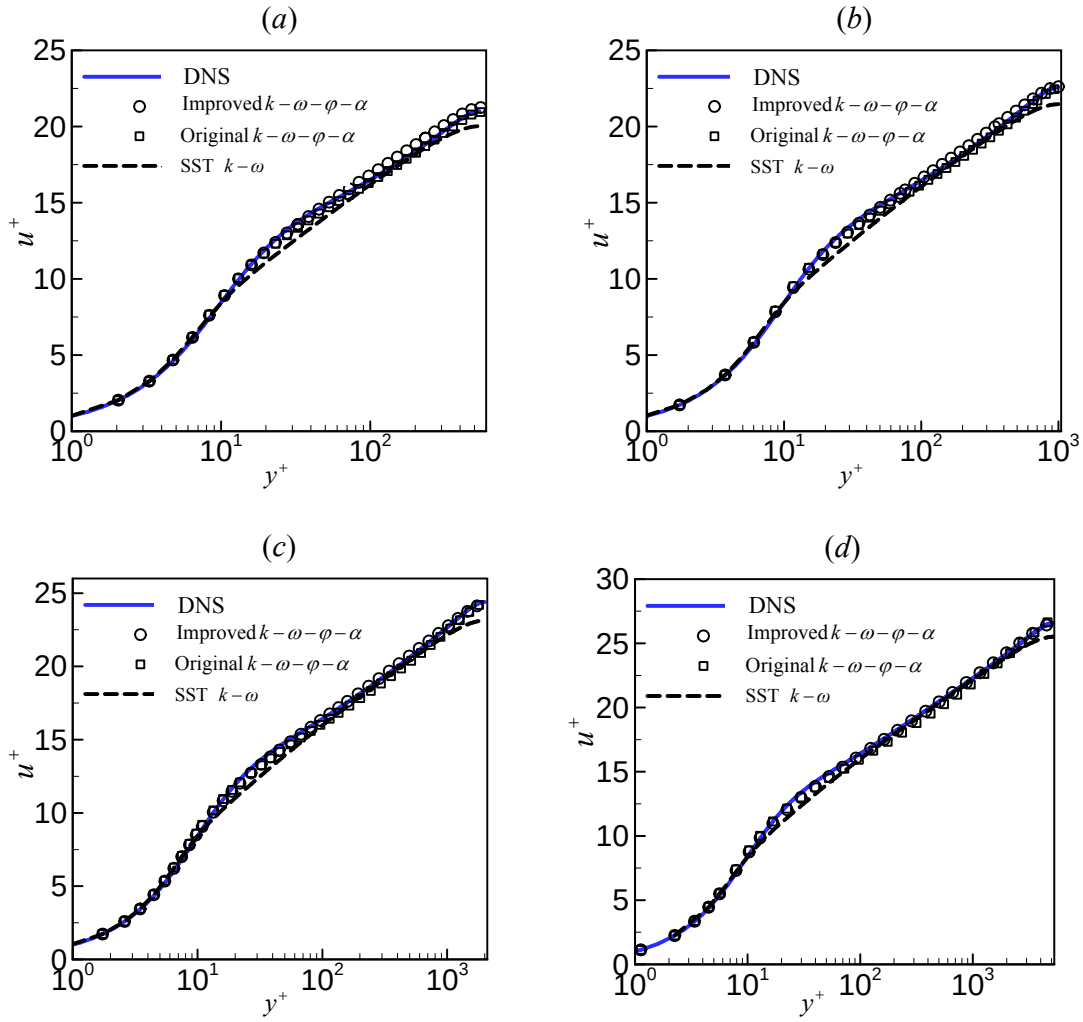
(a)
(b)
(c)
(d)
DNS
Improved $k-\omega-\varphi-\alpha$
Original $k-\omega-\varphi-\alpha$
SST $k-\omega$
u^+
y^+

Figure 2.

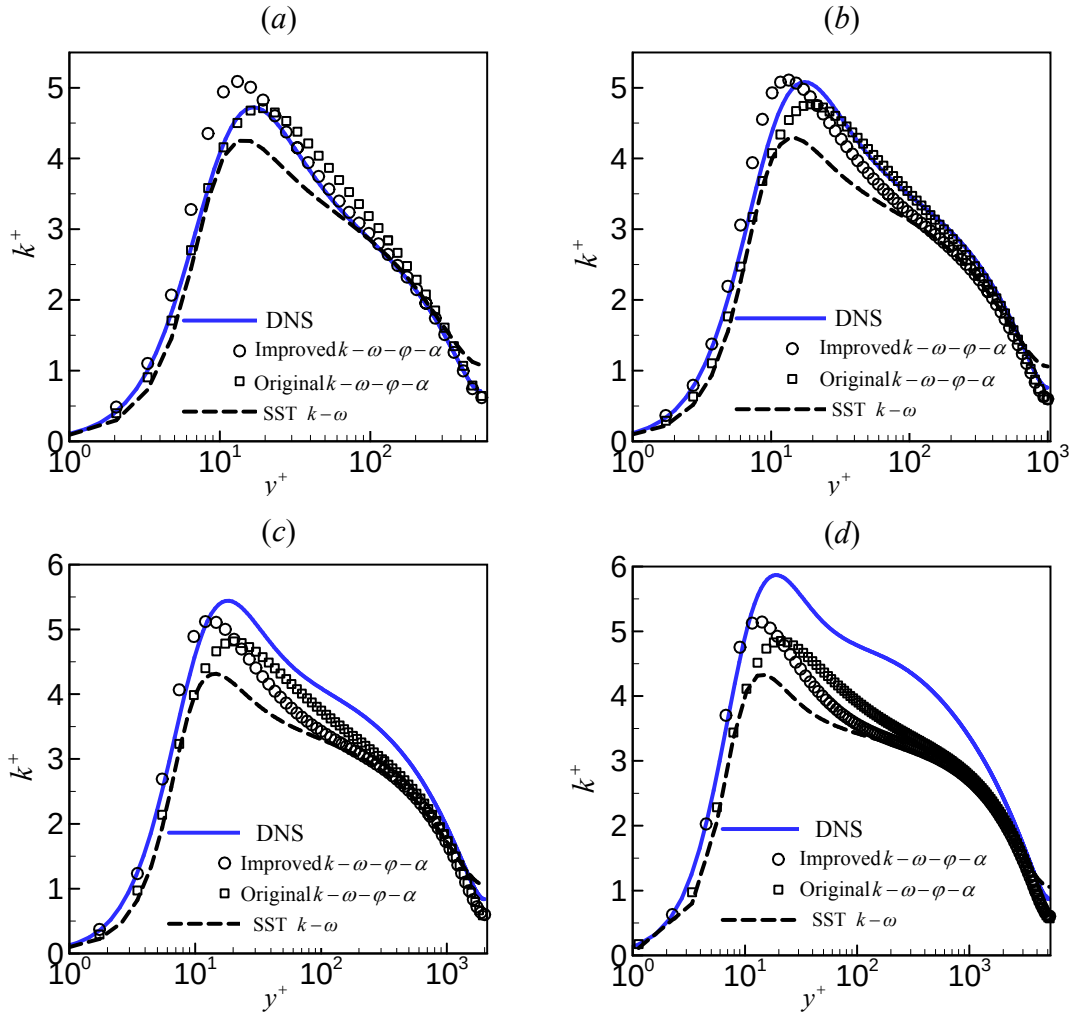
(a)
(b)
(c)
(d)
k^+
y^+
DNS
Improved $k-\omega-\varphi-\alpha$
Original $k-\omega-\varphi-\alpha$
SST $k-\omega$

Figure 3.

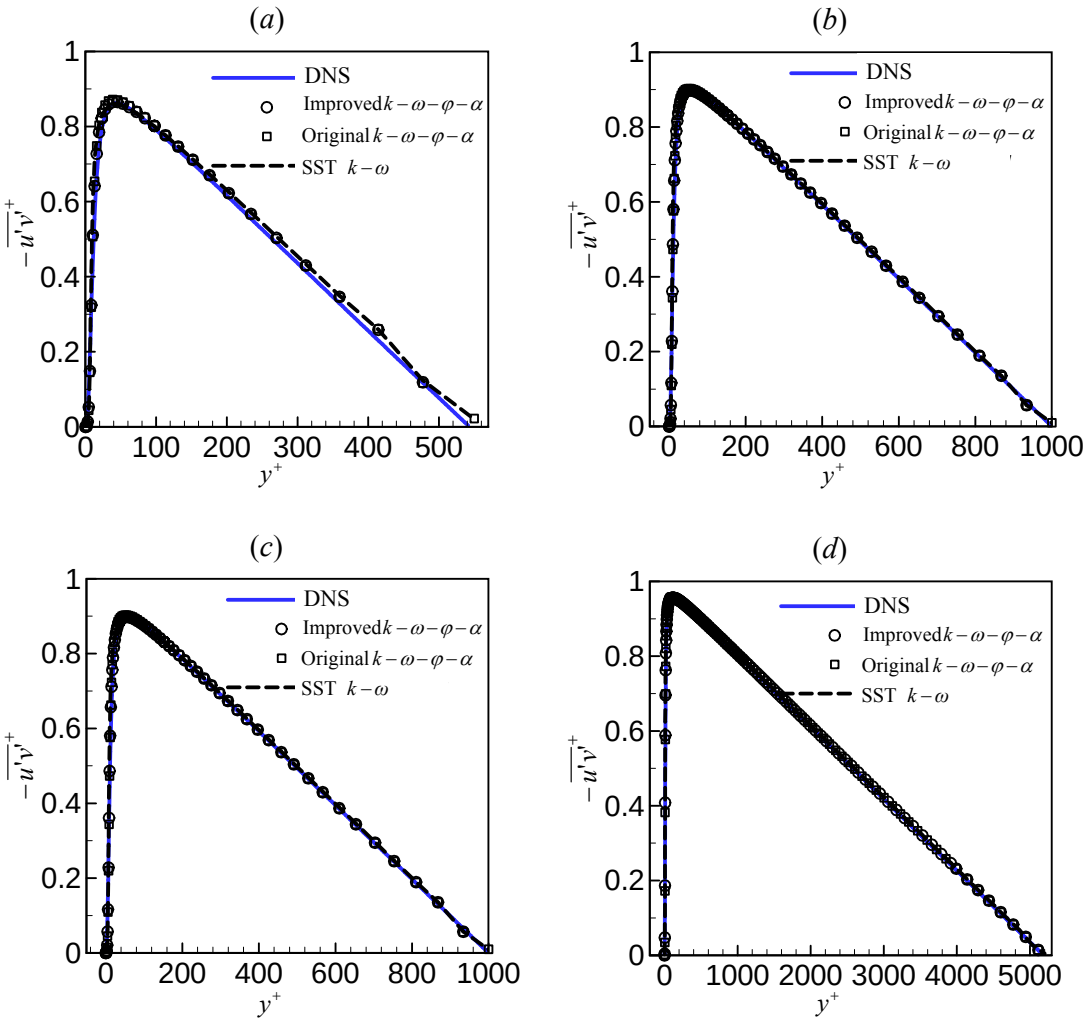
(a)
(b)
(c)
(d)
DNS
Improved $k-\omega-\varphi-\alpha$
Original $k-\omega-\varphi-\alpha$
SST $k-\omega$
$-\overline{u'v'}^{+}$
y^{+}

Figure 4.

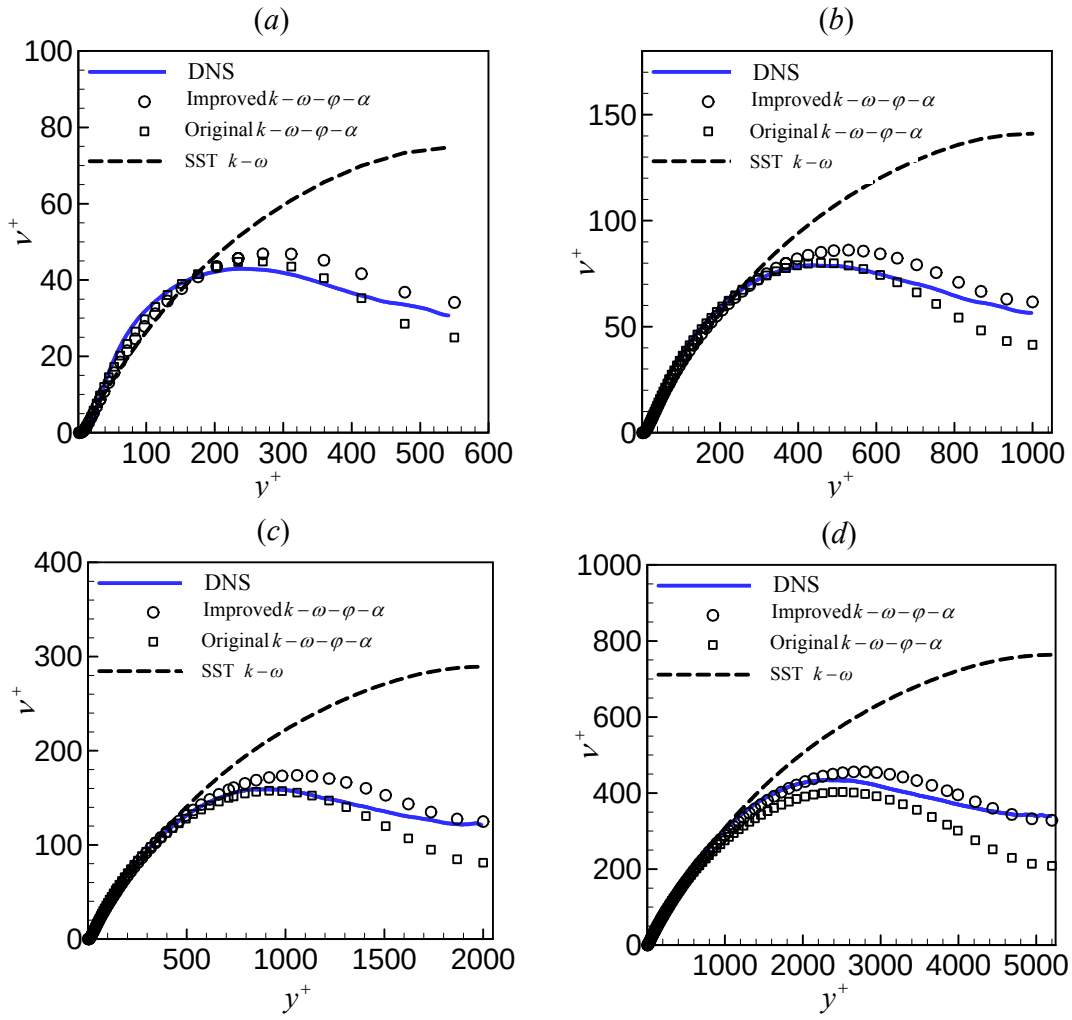
(a)
(b)
(c)
(d)
DNS
Improved $k-\omega-\varphi-\alpha$
Original $k-\omega-\varphi-\alpha$
SST $k-\omega$
v^+
y^+

Figure 5.

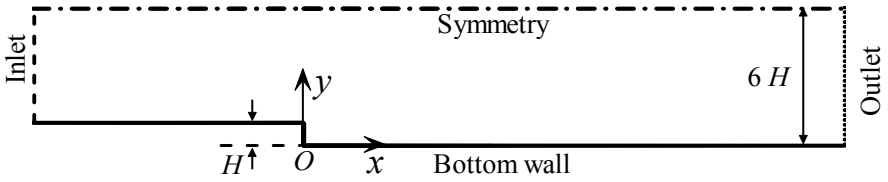

Figure 6.

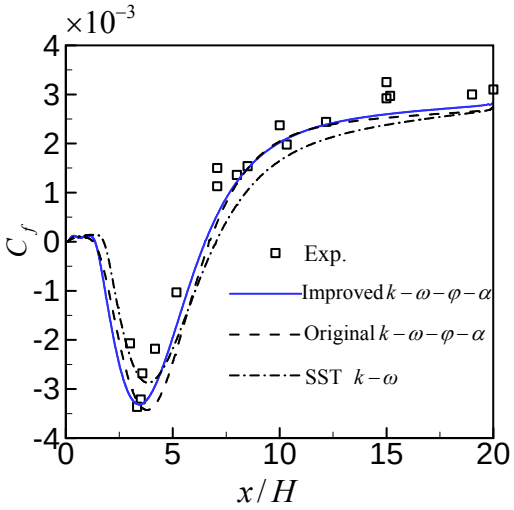

Figure 7.

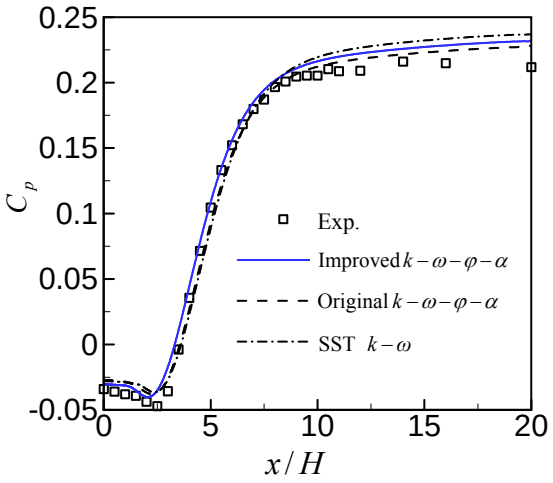

Figure 8.

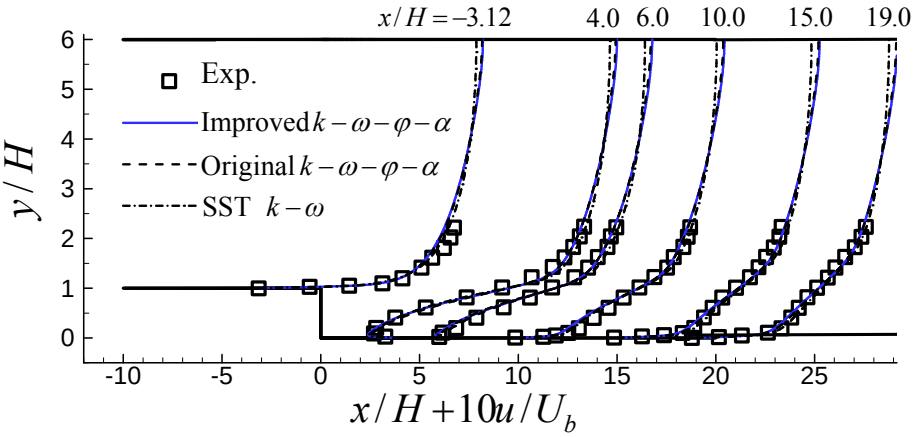

Figure 9.

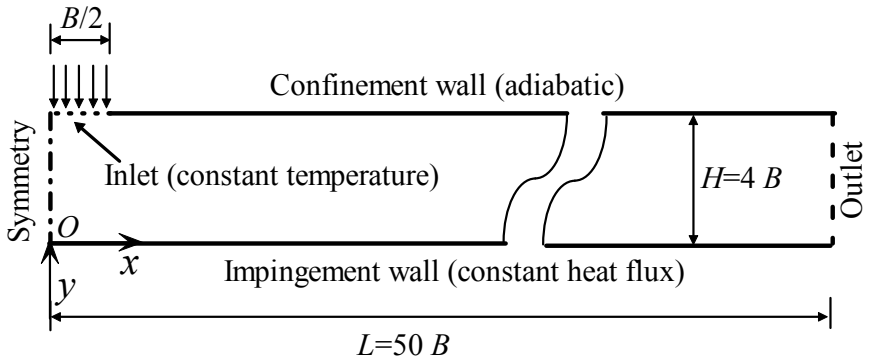

Figure 10.

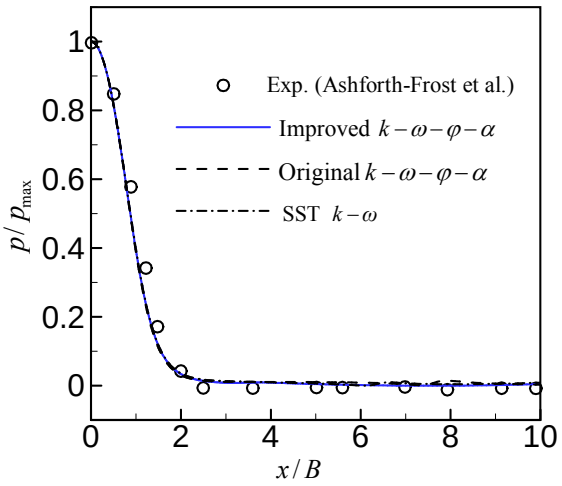

Figure 11.

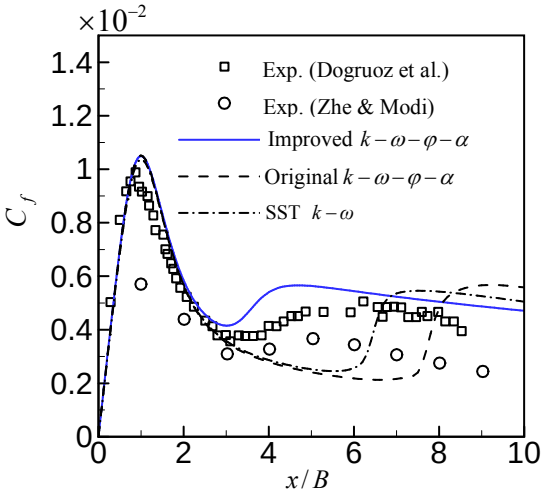

Figure 12.

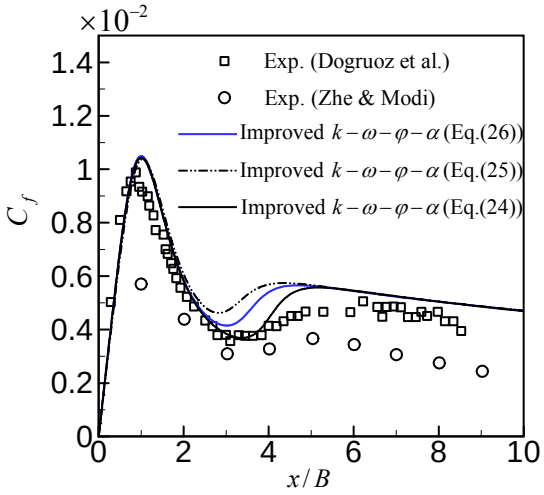

Figure 13.

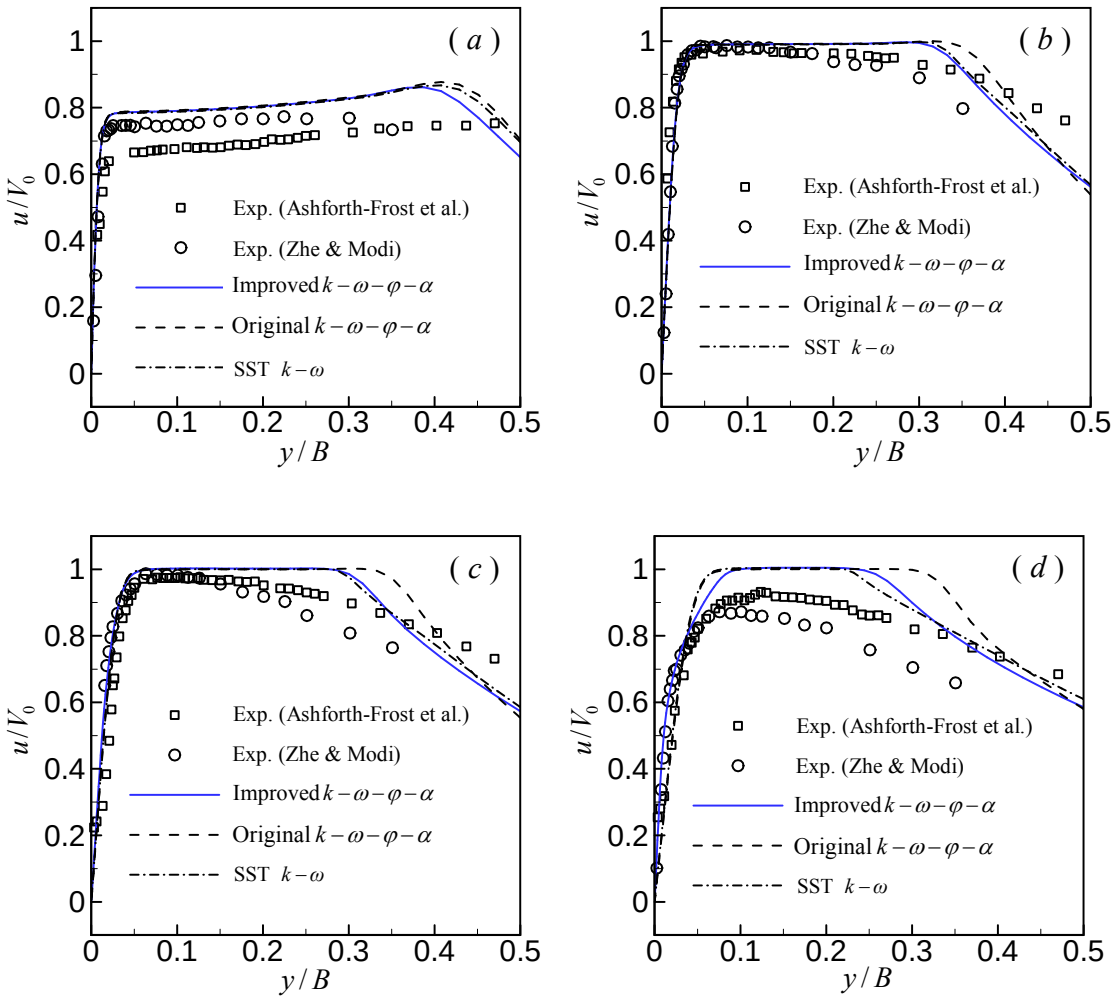

Figure 14.

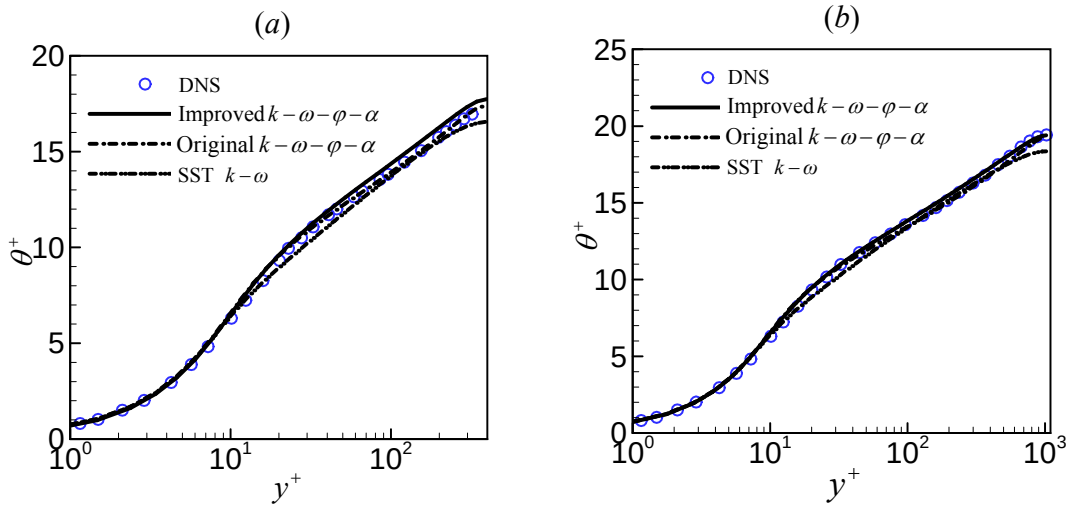

Figure 15.

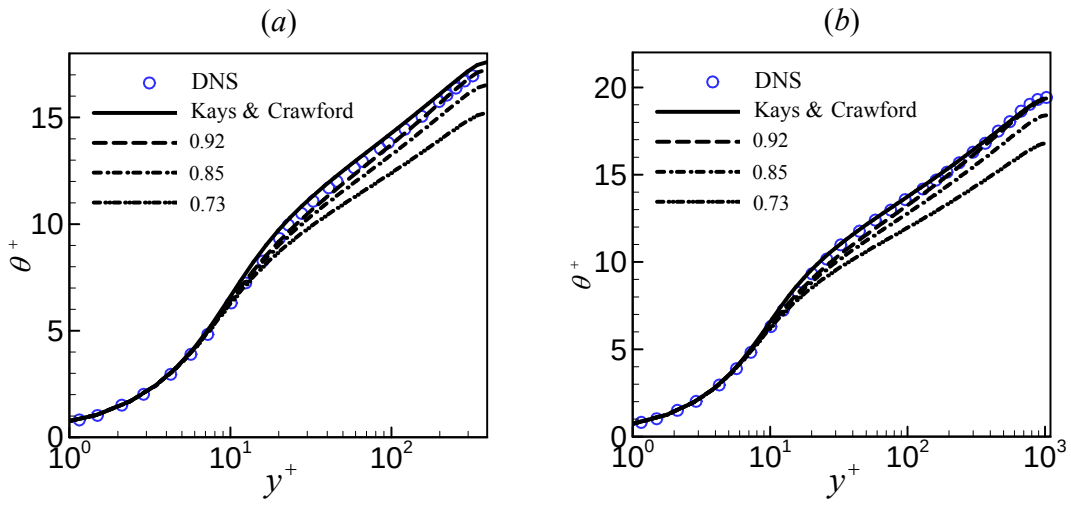

Figure 16.

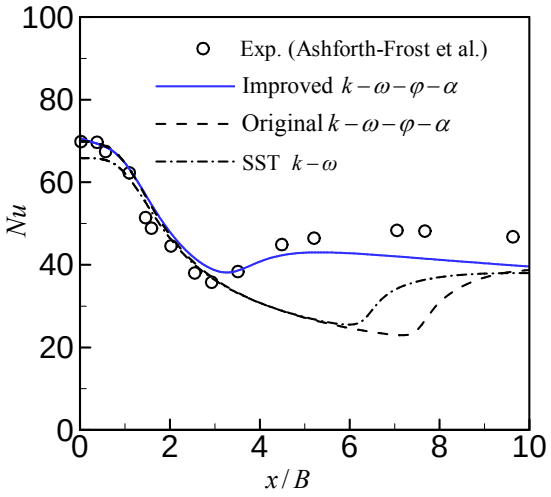

Figure 17.

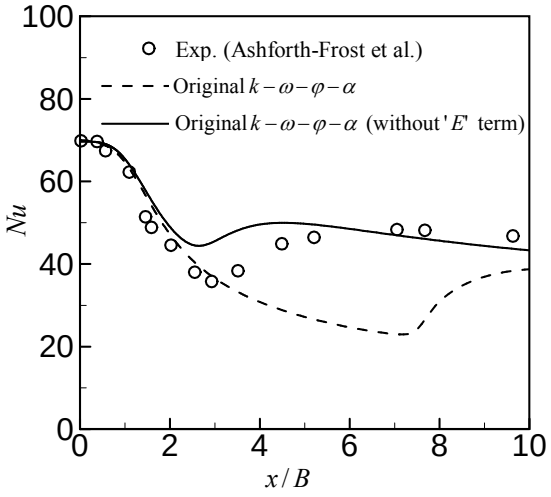

Figure 18.

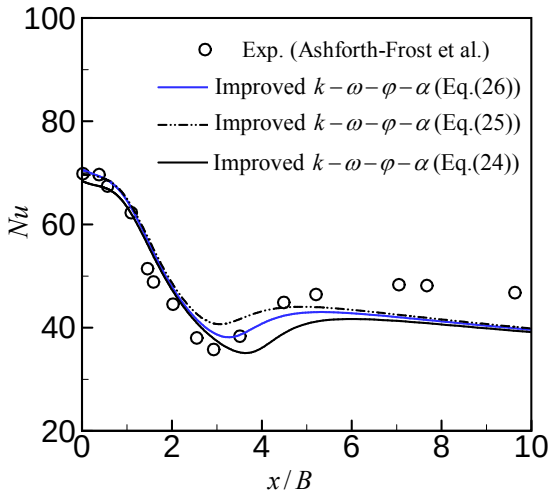

Figure 19.

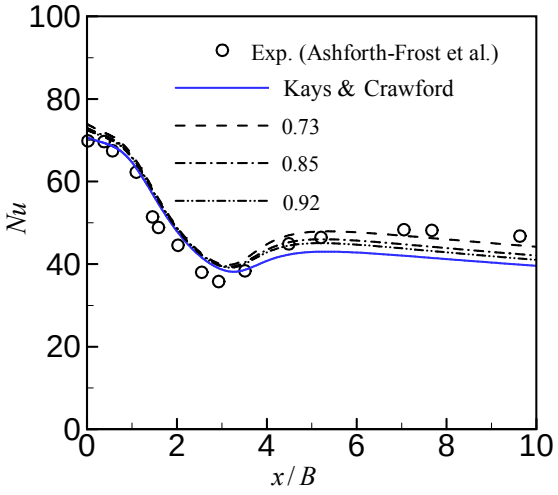

Figure 20.